Global Analysis of Direct Transfers from Lunar Orbits to Sun-Earth Libration Point Regimes

Josep J. Masdemont

IEEC & IMTech, Universitat Politècnica de Catalunya, Barcelona

Gerard Gómez

IEEC & Universitat de Barcelona, Barcelona

Liu Lei

Beijing Aerospace Control Center, China

Hao Peng

Rutgers, The State University of New Jersey, USA

February 16, 2021

Abstract

In this paper we look forward to obtain a global picture of simple transfer opportunities from Lunar to Sun-Earth libration orbits, useful for a preliminary design of these mission scenarios. Considering the trajectory of the Chinese Change'2 spacecraft as a reference case, the main transfer families are characterized and classified. In a second step, the results are analyzed and extended to departures from more general families of orbits about the Moon. Finally, we also include a preliminary sensitivity analysis of the first transfer correction maneuver (TCM1) to cancel injection errors. The methodology is of general applicability to the transfer analysis involving libration point final orbits in other general multi-body restricted systems.

1 Introduction

Since more than 40 years ago, libration point orbits (LPOs) have received much attention due to their particular location and environmental properties, that make them very suitable for space explorations. Among others, spacecraft such as ISEE-3, SOHO, Genesis, Herschel, Plank, Gaia, and Artemis have reached the Sun-Earth and Earth-Moon L_1 and L_2 points for scientific purposes [2]. Furthermore, LPOs also play a key role as staging nodes for low-cost transfers between the lunar LPOs and the collinear LPOs of the Sun-Earth system –the so called low-energy transfers– [3, 5, 15]. This kind of transfers can also be used as primary hubs for future human activities in the neighborhood of the Earth [5] or in the Solar System planetary and lunar explorations.

Periodic and quasiperiodic orbits of the restricted three-body model, as well as their invariant manifolds, are well-known dynamical structures that have been important tools in mission design. The main transfer examples include, Sun-Earth libration point missions [1,7], low-energy capture into Mars halo orbit [24,31], and transfers between collinear libration point orbits [4,12,14]. However, when the gravitational force-field created by any of the Sun, Earth,

and Moon cannot be ignored, the complexity increases [19, 20]. A simple way to deal with a four-body regime is to uncouple the model into two uncoupled three-body problems, i.e., the Sun-Earth-spacecraft and the Earth-Moon-spacecraft systems. Working this way, the above mentioned coupled models can still be used to approximate the design of transfers in the Sun-Earth-Moon system. This was the approach used in [17] to determine low-energy transfers between the Earth-Moon and the Sun-Earth systems. The spacecraft can be shifted from one system to the other by means of maneuvers executed at the intersections of two manifolds coming from different three-body regimes (see [10, 16, 17]). For the 2-dimensional transfers, in a planar restricted three-body problem (RTBP), the use of the Jacobi constant, together with a suitable Poincaré section, reduce the exploration of a 4-dimensional problem to 2-dimensional representations [16, 17] that can be easily visualized and used. For 3-dimensional transfer problems, Poincaré sections can still be used but the representation is not so easy. Earth-to-Moon transfers in the RTBP have been studied in [9, 25]. Transfers between libration points in a four-body coherent model have been studied in [19, 20].

The purpose of this paper is to analyze transfer orbits from the Moon to LPOs around the Sun-Earth L_2 equilibrium point, similar to the one performed by the Chang'e-2 spacecraft (CE-2). After completing its primary objectives, CE-2 successfully departed from the Moon on June 9th, 2011, and then orbited the Sun-Earth L_2 neighborhood [29, 32]. Several studies about the trajectory design of the extended mission of the lunar probe have been done. Qiao [29] constructed transfers searching intersection points of stable manifolds associated with the Sun-Earth L_2 Lissajous orbit and ballistic escaping trajectories from the Moon, he also found the actual flight trajectory used by CE-2. Wu [32] addressed the computation of the Lissajous trajectory insertion maneuver for the CE-2 spacecraft, while Nakamiya [23] investigated the characteristics of the connection between the departing points from the Moon and the stable manifolds of halo orbits in the Sun-Earth RTBP. However, a detailed map of all transfer opportunities between the Moon and the Sun-Earth libration point orbits including their features was not investigated in detail.

In this paper we consider a pure numerical approach to construct natural transfers from a lunar orbit, to the Sun-Earth L_2 libration point neighborhood, considering a realistic gravitational model extracted from the DE405 JPL ephemeris file. The procedure is based on obtaining shadowing trajectories to natural libration point orbits including their stable manifolds. We start implementing a first grid search method that is able to find trajectories that remain in the selected region for a relative long period of time (taking into account the instability of the zone in the Sun-Earth case we ask for, at least, 120 days). After this preliminary computation, and using the departure maneuvers at the Moon's orbit together with the departure epochs from the unstable region, the procedure enlarges the time spend by the first guess trajectory in the libration point region for a suitable period of time (about 450 days in our case) to confirm the candidate. Finally, by means of a bisection procedure, the 450-days libration point orbits are extended up to a long enough time (20 years in our case) to accurately determine and classify the libration point orbit that has been reached.

Some previous considerations about this same problem appeared in a previous paper [26], where the main goal was to show the performance of using GPUs under MATLAB in a computational intensive celestial mechanics problem based on a patched elliptic restricted three body model, well suited for the use of GPU's. In the present work we use real ephemerides and perform computational intensive explorations in a Linux Beowulf cluster in order to provide a general geometrical detailed analysis including parameter dependence and the sensitivity of

the transfer problem. A large amount of transfer trajectories have been obtained and analyzed, and two main kinds of transfer families have been identified. We discuss and present here their main features, including the distribution of transfer opportunities, amplitudes and the class of the final LPO. Finally, a preliminary sensitivity analysis of the first transfer correction maneuver (TCM1), to eventually reconstruct the target LPO in the presence of initial injection errors, is also addressed.

The methods developed and used in this paper can be easy extended to the Sun-Earth L_1, or to other libration point regimes, providing a global picture for the analysis of libration point transfers.

2   Review of the CE-2 libration phase mission

CE-2 was the second Chinese lunar exploration satellite, launched on Oct 1, 2010, it was injected into a 100-km altitude circular polar lunar orbit. In June 2011, the CE-2 mission was extended to explore the Sun-Earth L_2 libration point [22, 29, 32], taking full advantage of the remaining propellant and payloads.

According to its design, the target Lissajous orbit in the Sun-Earth rotating frame (defined in section 3), had x, y, and z-amplitudes of approximately 284,000 km, 880,000 km, and 367,000 km, respectively. The lunar departure was planned at 07:46:31 (UTC) on June 9, 2011, with a velocity increment of 680.85 m/s aligned with the current inertial velocity. However, constrained by the capacity of the CE-2 main thruster, the lunar escape maneuver was a continuous thrust performed in two steps and, consequently, larger than the one foreseen during the initial design. Fig. 1 shows the transfer trajectory and the final target orbit. The parameters of CE-2 lunar departing trajectory, in a Moon-centered J2000 reference frame, are given in Table 1 and they will be used as a reference in this paper. More details can be found in [22].
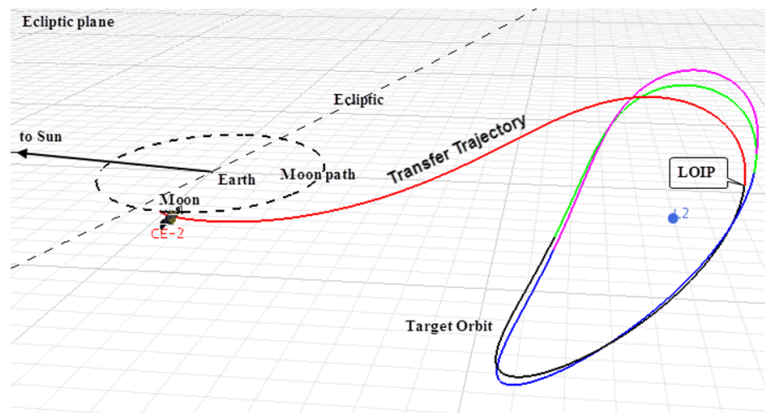

Figure 1: Scheme of the lunar escape orbit (left) and transfer trajectory (right) of CE-2 libration mission in Sun-Earth rotating coordinates [22]. The grid indicates the ecliptic plane.

	$a(\text{km})$	e	$i(°)$	$\Omega(°)$	$\omega(°)$	$M(°)$
09-06-2011, 7:46:31 UTC	1835.24	0.0094	83.54	260.26	4.93	81.28

Table 1: Moon-centered J2000 Keplerian elements of the CE-2 lunar departing orbit at epoch.

3 Model and methodology

We consider transfers from the Moon to a Sun-Earth libration point neighborhood in a restricted four-body model. The motion of the spacecraft is governed by Newton's equations, considering the gravitational forces of the involved Solar System bodies,

$$\boldsymbol{X}'' = G\left(m_S\frac{\boldsymbol{X}_S - \boldsymbol{X}}{\|\boldsymbol{X} - \boldsymbol{X}_S\|^3} + m_E\frac{\boldsymbol{X}_E - \boldsymbol{X}}{\|\boldsymbol{X} - \boldsymbol{X}_E\|^3} + m_M\frac{\boldsymbol{X}_M - \boldsymbol{X}}{\|\boldsymbol{X} - \boldsymbol{X}_M\|^3}\right), \tag{1}$$

were G is the gravitational constant, $\boldsymbol{X}$ is the position of the infinitesimal body in J2000 mean equatorial coordinates centered in the barycenter of the Solar System, $\boldsymbol{X}_{S,E,M}$ are the positions of the three Solar System bodies (Sun, Earth and Moon) obtained from the JPL ephemeris file DE405 in the same frame, and $m_{S,E,M}$ their masses. According to this data file, the values of the constants that we have used are: $Gm_S = 1.32712 \times 10^{11}$, $Gm_E = 3.98600436 \times 10^5$, and $Gm_M = 4.90280007 \times 10^3$ km^3/s^2. A Runge-Kutta-Fehlberg 7/8-order integrator has been used to propagate the trajectories, with a maximum local truncation error of 10^{-13}.

For some computations and illustrative purposes, the current inertial state $\boldsymbol{X} = (X, Y, Z) \in \mathbb{R}^3$ will be transformed into a synodic RTBP-like reference frame (Sun-Earth rotating coordinates), by means of the time dependent change of variables,

$$\boldsymbol{X} = kC\boldsymbol{x} + \boldsymbol{B} \tag{2}$$

where $\boldsymbol{x} = (x, y, z) \in \mathbb{R}^3$ denotes the position in this rotating RTBP-like coordinates [8]. In the above expression, $k = \|\boldsymbol{X}_S - \boldsymbol{X}_E\|$ is a scaling factor, C is an orthogonal matrix whose three columns, $\boldsymbol{C}_1$, $\boldsymbol{C}_2$, $\boldsymbol{C}_3$, are

$$\boldsymbol{C}_1 = \frac{\boldsymbol{X}_S - \boldsymbol{X}_E}{\|\boldsymbol{X}_S - \boldsymbol{X}_E\|}, \quad \boldsymbol{C}_3 = \frac{\boldsymbol{V}_E \times (\boldsymbol{X}_E - \boldsymbol{X}_S)}{\|\boldsymbol{V}_E \times (\boldsymbol{X}_E - \boldsymbol{X}_S)\|}, \quad \boldsymbol{C}_2 = \boldsymbol{C}_3 \times \boldsymbol{C}_1,$$

where $\times$ denotes the cross product, $\boldsymbol{V}_E$ is the velocity of the Earth with respect to the Sun, and $\boldsymbol{B} \in \mathbb{R}^3$ is a translation vector to set the origin at the barycentre of the Sun-Earth system.

As it is well known, in the circular RTBP there exist five equilibrium points, known as libration points, or Euler and Lagrange points. Three of them, L_1, L_2 and L_3, are unstable, while L_4 and L_5, for the case of the Sun-Earth mass parameter, are linearly stable [30].

In this work we are interested in the families of periodic (Lyapunov and halo) and quasiperiodic orbits (Lissajous and quasi-halo) around the collinear points L_1 and L_2. The structure of this central part of the phase space around the L_1 point is shown in Fig. 2, for a value of the Jacobi constant for which halo and quasi-halo orbits exist. The structure for the L_2 is very similar (see [8, 13]). The figure shows the intersections of the LPOs in the selected energy level with the (x, y) plane of the RTBP [8]. We see that, for the value of Jacobi constant considered, there is only one planar (horizontal) Lyapunov orbit (bounding the figure and completely contained in the (x, y) plane), one vertical Lyapunov, and two halo
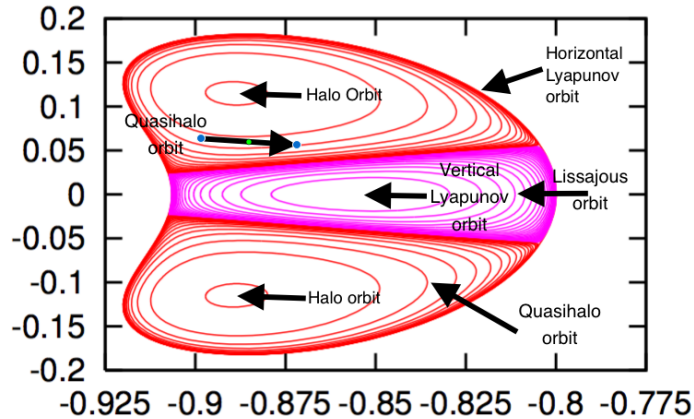
4

Figure 2: Poincaré map representation,of periodic and quasiperiodic orbits around the libration point L_1 of the Sun-Earth RTBP, in the usual (x, y) synodical coordinates and for a value of of the Jacobi constant within our interval of interest (JC=3.000785158).

periodic orbits, that correspond to the fixed points in the Poincaré section. Finally, families of Lissajous and quasi-halo orbits appear, which are represented by invariant curves about the vertical and halo orbits, respectively. Depending on the value of the Jacobi constant, other Poincaré maps can be obtained [8, 13] but the one considered in Fig. 2 summarizes the cases needed in our research. It is also important to remark that the representation of Fig. 2 corresponds to the RTBP, but it is also a good qualitative description for the dynamics of libration point orbits in a complete ephemeris model [21].

Previous works [10, 17, 18] indicate that there exist zero-cost transfers between Sun-Earth and Earth-Moon libration point regions. A spacecraft orbiting a Earth-Moon libration orbit can asymptotically reach a Sun-Earth libration orbit without any maneuver other than small guidance and navigation controls [2]. Based on these results, we are going to define a libration point region in the Sun-Earth system where we expect that a trajectory escaping from the lunar orbit can enter and remain inside it for a relatively long time, taken into account the unstable character of the zone. The approach starts from a grid search computation where suitable candidates are refined in successive steps up to the point that their final LPO orbits can be classified and analyzed.

3.1 Libration point region and grid search

Let $\Delta \boldsymbol{v} \in \mathbb{R}^3$ be the departure maneuver from the lunar orbit, performed at epoch t_d with the purpose of transferring the spacecraft to a Sun-Earth LPO. The direction of this maneuver is defined by two angles, α and β, in the body-centered velocity coordinate frame, as shown in Fig. 3. In this reference frame, the current inertial velocity $\boldsymbol{v}$ of the spacecraft defines the ξ-axis direction, the η-axis is parallel to the normal direction to the orbital plane and the ζ-axis completes a right-handed reference frame. In this way, if Δv denotes the magnitude of the maneuver $\Delta \boldsymbol{v}$, then

$$\Delta \boldsymbol{v} = \Delta v \cdot \left(\cos \alpha \cos \beta, \, \sin \alpha \cos \beta, \, \sin \beta \right)^T . \tag{3}$$
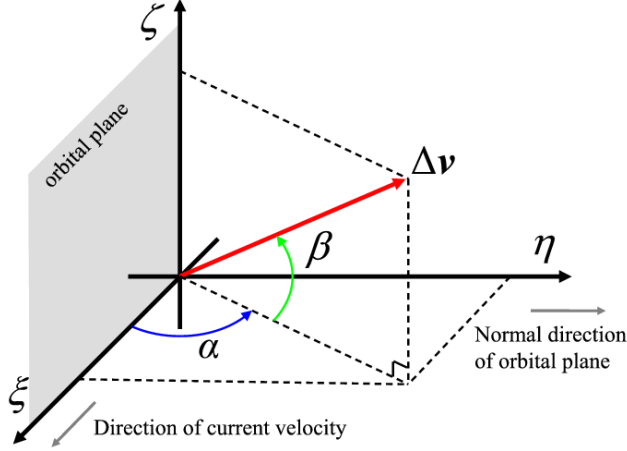
5

Figure 3: Representation of the angles α and β, in the body-centered velocity frame, defining the departure maneuver Δv from the lunar orbit. The orbital plane is the instantaneous orbital plane of the lunar polar orbit at the epoch of the departure maneuver.

For natural reasons of efficiency, most of our work is going to consider tangential aligned departure maneuvers, i.e., $\alpha = \beta = 0$, and, as it has been stated in the introduction, a test-bed for our computations will be the Chang'e-2 extended mission to the Sun-Earth L_2 point. Taking the Keplerian elements of CE-2, provided in Table 1, we can easily obtain the state of this particular spacecraft just before the lunar departure.

To start with the methodology, let us consider $\boldsymbol{X}_d^- \in \mathbb{R}^6$ a state previous to the departure maneuver, and a departure maneuver Δv, in such a way that $\boldsymbol{X}_d = \boldsymbol{X}_d^- + (0_3, \Delta v)$ is the departure state of a simulation. This state is propagated forward in time, up to 500 days, using equations (1). The length of the propagation has been selected so that the trajectory has more than time enough to reach the Sun-Earth libration point vicinity.
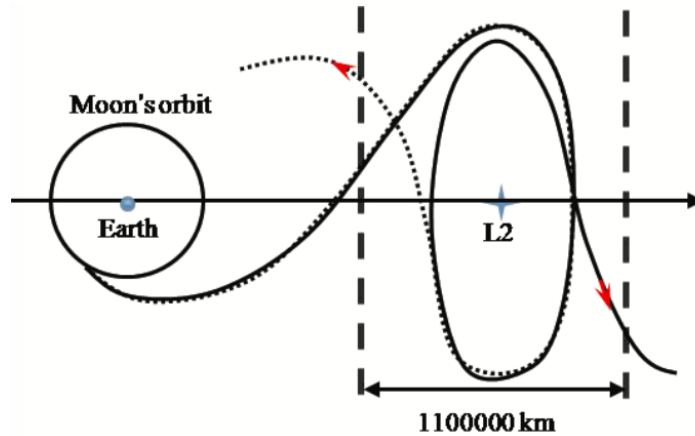

Figure 4: Qualitative representation of the selected LPO region about the Sun-Earth L_2 point in synodical coordinates. The region is the band bounded by the dashed lines.

The method to compute transfer trajectories makes use of the time interval T_d that a trajectory remains inside a selected neighborhood of the libration point. From now on, this neighborhood will be called the *LPO region*. Due to the existence of zero velocity curves limiting the y component of the set of LPOs, and also to the fact that an orbit escaping from the libration point shadows the unstable manifolds of LPOs, only the x component is needed to define this LPO region as a band domain centered at the target libration point, as is shown in Fig. 4. At each integration step, the current state is transformed into a synodic RTBP-like reference frame (Sun-Earth rotating coordinates), by means of the time dependent change of variables (2) in order to check if the spacecraft is inside this selected region.

The width of the LPO region has been determined requiring that it contains all the periodic and quasiperiodic orbits of interest (see Fig. 2). For the Sun-Earth system, the upper and lower boundaries for the x component of the region are 5.5×10^5 km away from the target L_2 point (for the L_1 case the size of the LPO region would be the same).

Given a nominal lunar orbit, such as the one of CE-2, for the computation of possible transfer trajectories we discretize the set of variables $(t_d, \Delta v)$. Each departure state $\boldsymbol{X}_d = \boldsymbol{X}_d^- + (0_3, \Delta \boldsymbol{v})$ is propagated up to its, eventual, first intersection with the LPO region at a certain epoch t_{in}. The integration continues until the orbit leaves the LPO region at t_{out}. In order to reject those orbits that only pass by the LPO region rather than approaching to a LPO, a minimum value for $T^0 = t_{\text{out}} - t_{\text{in}}$, has been set. For this first step $T^0 = 120$ days, which is, approximately, half of the period of a typical Sun-Earth LPO. In the procedure, if $T > T^0$, the corresponding initial condition of the grid search is recorded and considered to be a transfer candidate, otherwise the grid point is rejected. It is also worth to point out that there can be multiple epochs for a trajectory to enter into the LPO region, this possibility has also been considered.

The grid size for this first exploration has been of $\delta t = 10$ minutes for the departure time t_d (within the whole year 2011), and of $\delta v = 40$ cm/s for the magnitude of the initial maneuver Δv (within the interval [640 m/s, 720 m/s]). The set of recorded pairs $(t_d, \Delta v_d)$ of this grid produce trajectories that remain inside the LPO region for at least $T^0 = 120$ days.

3.2 Refinement of transfer candidates

The purpose of this subsection is to explain the refinement procedure of the initial transfer candidates determined in the previous step, and the method to maintain the resulting orbit inside the LPO region for a time interval of about 450 days. This ensures that the orbit, without any correction maneuver, inside the LPO region is close enough to a certain LPO. Due to the exponential instability of the orbits in this region, and the numerical accuracy of the computations, we cannot expect much longer time intervals.

Tuning the magnitude Δv of the departure maneuver at the lunar orbit, the final end of the trajectory is either exiting the LPO region around the equilibrium point through the left hand side line (going back towards the Earth) or through the right hand side line (going away from the Earth). The procedure to enlarge the total time spent by the orbit within the band takes advantage of this fact. Slightly increasing or decreasing the grid value for Δv, two initial velocities, $\boldsymbol{V}_d^-$ and $\boldsymbol{V}_d^+$ are obtained, such that the associated trajectories exit the LPO region through any of the boundaries. Between both, there should be a transfer trajectory remaining in the LPO region for a maximal time interval. This trajectory is detected by means of an iterative procedure.

Let $(t_d, \Delta v_d)$ a point of the grid such that the orbit associated to it remains in the LPO region at least for a time T^0. In the iterative method to enlarge the final time up to $T^1 > T^0$, the value of Δv_d is refined, keeping fixed the departure epoch t_d with the associated $\boldsymbol{X}_d^-$ state on the lunar orbit. At each iteration the time spent by the orbit within the LPO region is increased, until it reaches the desired value T^1 which has been taken equal to 450 days.

Denote by $\Delta v_d^0 = \Delta v_d$ and $\delta v^0 = \delta v / N$ the initial values for the refinement of $(t_d, \Delta v_d)$, where N is a fixed number for all the iterations. We have used $N = 8$ for almost all the explorations, so $\delta v^0 = 5$ cm/s for the refinement of the candidates.

Defining $\delta v^k = \delta v^{k-1}/N$, at the iteration number k the initial conditions associated to the following $2N + 1$ values of $\Delta v_d \in [\Delta v_d^k - \delta v^k, \Delta v_d^k + \delta v^k]$:

$$\Delta v_i = \Delta v_d^k + i\frac{\delta v^k}{N}, \quad i = -N, -N+1, ..., 0, 1, ..., N,$$

are propagated. The largest value obtained for the time spent by the orbit within the LPO region in the $2N + 1$ propagations is set equal to T^k. The iterations finish when either the value of T^k is larger than T^1, or when a maximum number (usually set to three iterations) is reached. It has been seen that most of the transfer candidates that fail this time-enlargement procedure are in fact transient orbits (see [10]) through the LPO region.

The 450 days requirement approximately corresponds to 2.5 periods of a typical Sun-Earth L_2 LPO, and has been determined after some trial-and-error tests to ensure both a long enough duration time inside the LPO region, and an acceptable computational cost of the search procedure.

3.3 Extending the time interval within the LPO region

Our main interest is the classification of the LPO reached by the transfer trajectory, either as a halo, quasihalo or Lissajous orbit. Due to the exponential instability character of LPOs, and the limitation in the accuracy of the computations, we cannot obtain a transfer trajectory remaining in the LPO region for an arbitrary long time interval (the required initial changes in the departure maneuver would be much smaller than the accuracy for the representation of the initial state). However, the idea of the previous bisection procedure can still be applied for these extensions. In our work, the refined 450-day orbits have been extended up to 20 years inside the LPO region. The procedure is as follows:

1. Let t_1 and $\boldsymbol{X}_1$ be the epoch and the state when the transfer trajectory crosses the left boundary of the LPO region for the first time.

2. Propagate $\boldsymbol{X}_1$ forward in time during 90 days (about half a period of a typical Sun-Earth LPO). Denote the terminal epoch and state by t_2 and $\boldsymbol{X}_2$, respectively. Recall that if $\boldsymbol{X}_2$ would be propagated forward in time, the trajectory would remain inside the band region for, at least, 450-90=360 days, but this extra arc is not considered by now.

3. Using t_2 and $\boldsymbol{X}_2$ as a new initial state, apply a bisection procedure to enlarge the duration time inside the LPO region of the remaining trajectory segment. The trajectory departing from the new state $\boldsymbol{X}_2^*$, (close to $\boldsymbol{X}_2$) will remain inside the band region for, at least, 450 days more (i.e. at least up to time $T = t_2 + 450$ days). Recall that, according to the bisection procedure, the positions of $\boldsymbol{X}_2$ and $\boldsymbol{X}_2^*$ will be the same.

4. If the total time T inside the LPO region is longer than the 20 years requirement, then stop the procedure. In this case one can proceed to compute the characteristics (orbit class and amplitudes) of the reached LPO.

5. If $T < 20$ years, then update $(t_1, \boldsymbol{X}_1)$ with $(t_2, \boldsymbol{X}_2^*)$, and go to Step 2.

Note that the above procedure produces a "trajectory" with velocity discontinuities from $\boldsymbol{X}_2$ to $\boldsymbol{X}_2^*$, each time the iterative bisection method is applied, this is, approximately every 90 days. However, these discontinuities are so tiny (on the order of 10^{-5} m/s, or even smaller) that cannot be considered as station keeping maneuvers, but as a shadowing of a real LPO (understood in the sense of the *shadowing lemma* in dynamical systems theory). These tiny adjustments in velocity are used to avoid the instability in the libration point region and to determine the final orbit characteristics. In fact, the resulting "natural" LPO is determined with an accuracy similar to that we would obtain using other numerical refinement or generating schemes, like a multiple shooting method [6].

4 Transfer opportunities and final LPOs for Chang'e-2

Using the approach of the preceding section, we have analyzed the feasible transfers from the lunar polar orbit used by the CE-2 spacecraft to a libration point orbit about the Sun-Earth L_2 point, in the next section we study other departing lunar orbits. The set of initial departure states has been taken in a grid of two of the four variables that define it, since the departure maneuver is always assumed to be tangential, i.e. $\alpha = \beta = 0$.

The state $\boldsymbol{X}_d^-$ is converted from the orbital elements of the lunar CE-2 orbit, given in Table 1, to position and velocity in a Moon-centered reference frame. Since CE-2 departed from the lunar orbit in June 2011 [22], we have explored departing epochs t_d within the whole departure year 2011 (between 2011/01/01/00:00 and 2011/12/31/23:59 UTC). The time step for the exploration of this time interval has been set equal to 10 minutes.

The selection of the interval for the departure maneuver Δv has been taken large enough to include all the values between the Jacobi constant J_C of the lunar polar orbit and the one of a LPO, considering possible variations of J_C due to other solar system bodies. We estimated it to be [640 m/s, 720 m/s], and the exploration step of this interval has been taken equal to to 0.4 m/s.

Within these two intervals for t_d and Δv, we have a complete initial grid search with more than 10,000,000 potential transfer trajectories. At each grid point the resulting initial departure condition $\boldsymbol{X}_d$ has been propagated for more than 450 days, in order to ensure that the trajectory has enough time to reach the LPO region. The potential transfers that pass the two screening processes (the initial one requiring to remain 120 days inside the LPO region, and the subsequent refinement to more than 450) are recorded as feasible initial conditions for the transfer.

This initial search procedure detects a huge number of transfer candidates fulfilling the above requirement (the associated computation, implemented in Fortran, under a Linux blade of our computing cluster, takes about 75 h of CPU time when running in a core of an Intel Xeon 2.4GHz processor). The candidates are displayed in Fig. 5. Each point in the figure represents the departure maneuver Δv in front of the departure epoch t_d of a successful transfer. The marks are colored according to the time of flight (t_{FT}) required to reach the
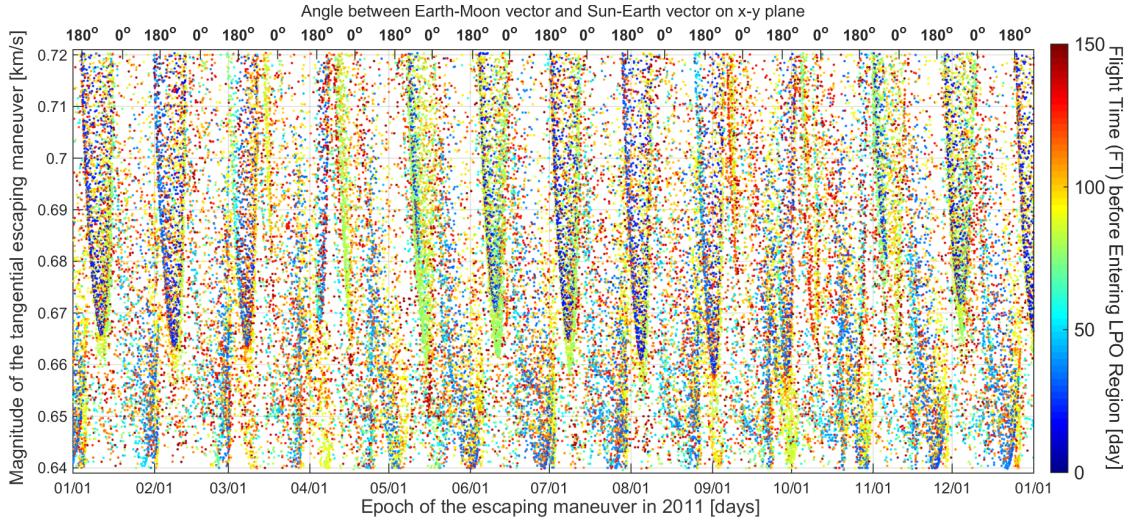
9

Figure 5: Cost (in km/s) of the transfer opportunities, detected by the initial search procedure during the year 2011, departing from an almost polar orbit around the Moon to a LPO around the L_2 point of the Sun-Earth system. The dots are colored according to the time of flight required to reach the LPO region. The x-axis ticks on the top give the angle between the Earth-Moon and the Sun-Earth directions at the departure epoch t_d.

LPO region, which varies from about two weeks up to 150 days. In the upper part of the figure, approximately in a monthly basis period, there appear parabolic-shaped dense regions. Between these parabolic regions, there are also dense regions of transfer opportunities in the lower part of the figure, again with periodicity of about one month. These two differentiated periodic regions provide different kinds of transfer orbits.

The periodicity patterns detected in Fig. 5 become clearer if we represent in different plots the transfer initial conditions associated to different times of flight. This is done in Fig. 6, where the total time of flight interval has been split in five subintervals of different length. Transfers taking a longer time of flight before reaching the LPO region ($t_{FT} \in [93, 150]$ days) are displayed in the two upper plots of the figure. These transfers involve several revolutions around the Earth and/or Moon encounters before reaching the LPO region. Some sample orbits of this kind of transfers are shown in Fig. 7 (right), and we refer to them as *multi-encounter transfers*. The dots in these two plots are distributed rather uniformly along the year, without displaying a clear periodicity. It should be noticed that, although these transfers are slow, they are not cheap in terms of the Δv required. In what follows we are going to discard these multi-encounter transfers.

The transfer orbits associated with the three lower plots in Fig. 6 reach the LPO region more straightforward (without wandering and close encountering with either the Earth or the Moon). Two of these orbits are shown in Fig. 7 (left), and we will refer to them as *direct transfers*. When $t_{FT} < 43$ days, or $t_{FT} \in [68, 92]$ days, the periodic pattern is much more clear. Since, from a practical point of view, 43 days is a reasonable maximum transfer time to the LPO region, we mainly consider this subset of direct transfers.

According to the bottom plot of Fig. 6, there are two different families of transfers with $t_{FT} < 43$ days: *Family I*, in the lower part of the plot (light blue), and *Family II*, with clear
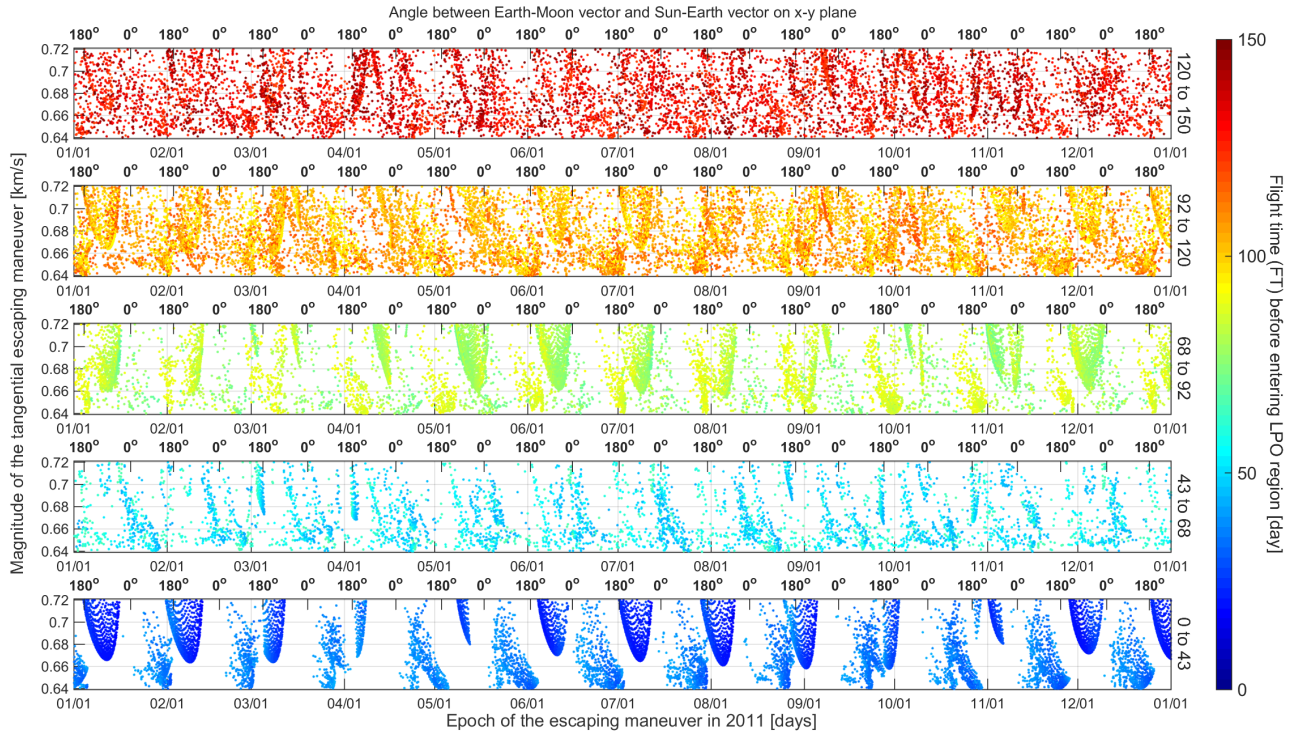
Figure 6: Departing epoch vs departing maneuver Δv, associated to transfer orbits grouped according to the time of flight required to reach the LPO region. Both the colors and the ticks used are the same as in Fig. 5.

parabolic boundaries, in the upper part (dark blue). The pattern of both families is roughly repeated with a periodicity of about one month, as a natural consequence of the periodic motion of the Moon about the Earth. To clearly show this fact, the initial phase angle $\theta(t_d)$ between the Earth-Moon and the Sun-Earth directions (projected on the ecliptic plane), and defined according to Fig. 8, at the departure epoch t_d is displayed on the upper x-axis of Figs. 5, 6 and 9. Looking to the values of $\theta(t_d)$, it is clear that *Family I* is centered around $\theta = 90°$ and *Family II* around $270°$. The two collinear Sun-Earth-Moon configurations, corresponding to $\theta = 0°$ and $180°$, appear to be, approximately, at the boundaries between the two families. The lowest values of Δv for *Family I* correspond to these collinear configurations, and those for *Family II* seem to be associated to the two orthogonal configurations $\theta = 90°$ and $270°$. There appear also some seasonal dependence about April, May, October and November where the density of direct transfers significantly decreases. This seasonal dependence, for transfers with a time of flight less than 43 days, will be clearly corroborated in similar figures of section 5.

Fig. 9 shows with some more detail a two-month time interval of initial conditions around the departing day of CE-2 (June 9th, 2011) which is also pointed out in the figure. The remarks that follow, related to Families I and II within this two-month interval, also apply to the other intervals.

Generally speaking, when comparing *Families I* and *II*, transfers in *Family II* require
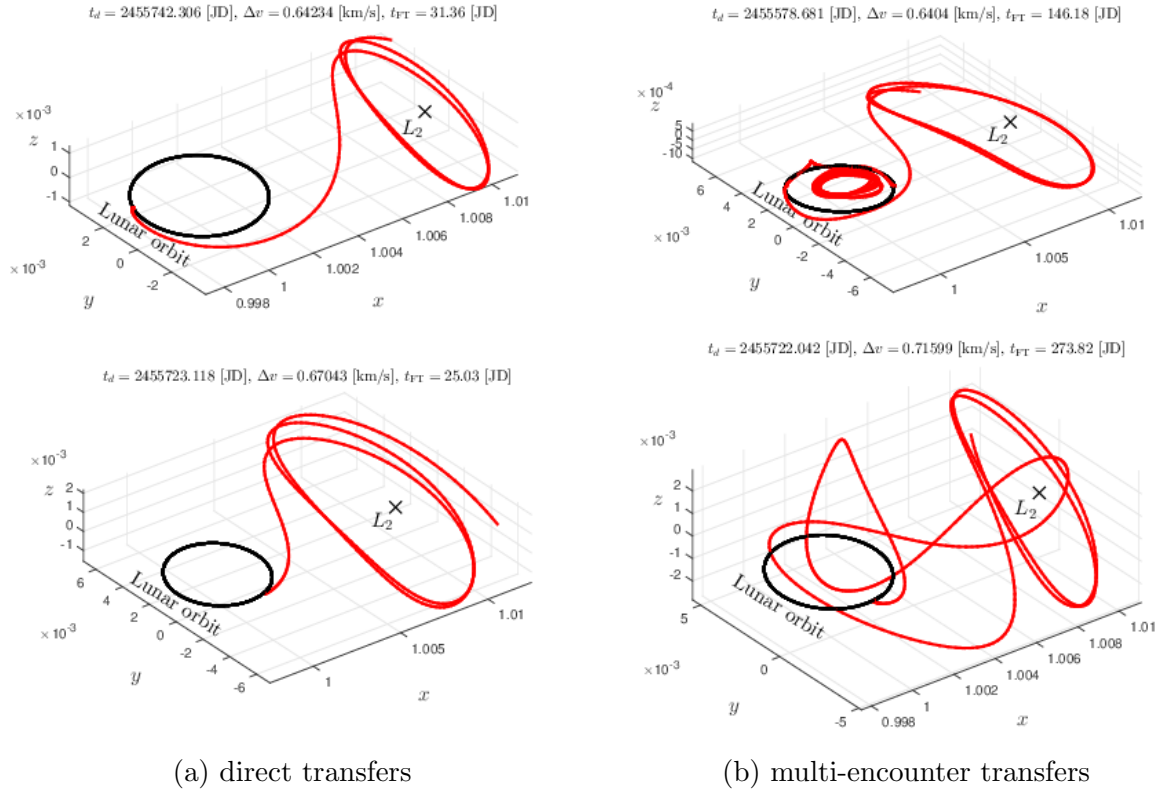
11

$t_d = 2455742.306$ [JD], $\Delta v = 0.64234$ [km/s], $t_{\mathrm{FT}} = 31.36$ [JD]

$t_d = 2455578.681$ [JD], $\Delta v = 0.6404$ [km/s], $t_{\mathrm{FT}} = 146.18$ [JD]

$t_d = 2455723.118$ [JD], $\Delta v = 0.67043$ [km/s], $t_{\mathrm{FT}} = 25.03$ [JD]

$t_d = 2455722.042$ [JD], $\Delta v = 0.71599$ [km/s], $t_{\mathrm{FT}} = 273.82$ [JD]

(a) direct transfers　　　　　　　　(b) multi-encounter transfers

Figure 7: Examples of direct (left) and multi-encounter (right) transfers. The multi-encounter transfers perform intermediate revolutions around the Earth, or have close encounters with the Moon or the Earth. The direct transfers go directly to the LPO region after departing from the orbit around the Moon. In all the plots the length unit is the Sun-Earth distance.
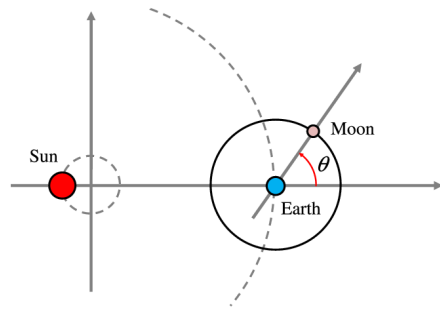
Figure 8: Qualitative representation of the Sun-Earth-Moon system geometry at the departure epoch t_d. The phase angle θ is zero when the Moon is collinear with the Sun and the Earth at the right of the Earth position. The angle θ is measured counterclockwise from zero value.
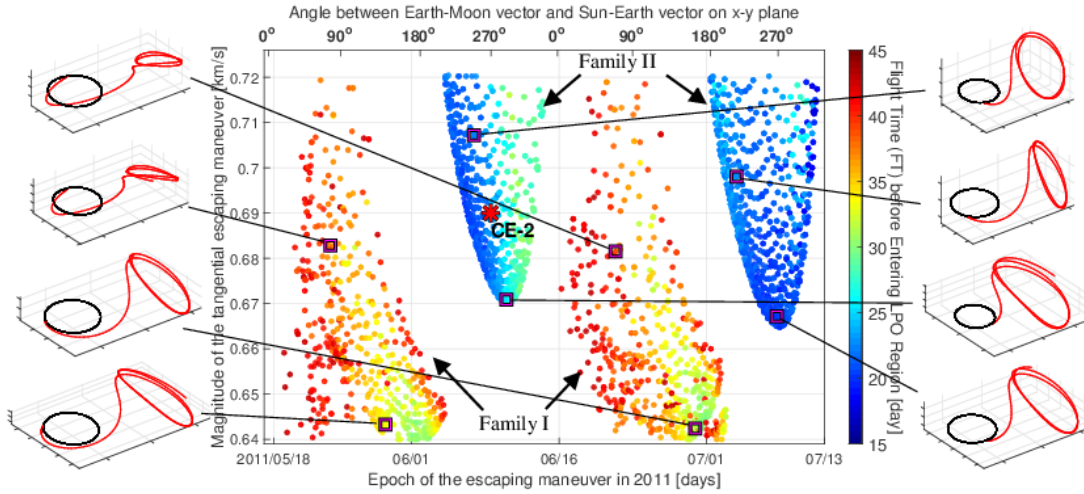
Figure 9: Departing epochs and maneuvers associated to direct transfer *Families I* and *II*, with times of flight less than 43 days (colored from 15 to 45 days). The red asterisk stands for the departure epoch and the magnitude of departure maneuver of the CE-2 [22]. Some transfer orbits of *Families I* and *II* are shown using Sun-Earth RTBP units. The black circular orbit displayed with the plots of the transfer trajectories represents the lunar orbit.

higher departure maneuvers but shorter time of flight. However, transfers in the bottom part of *Family I* require longer values of $t_{\rm FT}$ and need less Δv, while transfers corresponding to the upper part of *Family I* need both larger $t_{\rm FT}$ and Δv. Fig. 9 also illustrates the different behaviors of the transfer orbits of these two kinds of direct transfers.

Looking at the transfers in *Family II*, it seems that when the departure starts from the half x-y plane with $y < 0$, the value of Δv is similar to the one of the *Family I*. According to [27], this can be explained analyzing the inertial energy variation of the trajectory in the Sun-Earth and Earth-Moon RTBP models, since the energy is reduced when the trajectory moves in the half x-y plane with $y < 0$. Finally, as is shown in Fig. 9, we notice that the CE-2 probe was foreseen to depart from the Moon on June 9th, 2011 using a *Family II* transfer trajectory.

4.1 Classification of the attained LPOs

In order to have a better understanding of the relationship between the departure epoch t_d, the departure maneuver Δv, and the final libration point orbit (LPO) reached, we have classified the final LPOs according to their dynamical behavior.

Although all the libration point orbits have been computed in a restricted 4-body full ephemeris model, their qualitative behavior is analogous to the LPOs of the RTBP; taking into account that, in the 4-body model there are no longer periodic orbits and the bounded orbits we find are all quasiperiodic. Leaving aside some chaotic motions, in the RTBP there are two kinds of bounded orbits: periodic and quasiperiodic, as is shown in Fig. 2. The main periodic orbits are the planar and vertical Lyapunov orbits, as well as the halo orbits, while the quasiperiodic orbits can be of the Lissajous or the quasi-halo type. All, periodic and quasiperiodic, can be characterized by their in-plane A_y and out-of-plane A_z amplitudes.

13

Since the LPOs reached by the transfer orbit have been computed for a very long time interval, as explained in Section 3.3, they are easy to be classified in an automatic way as follows.
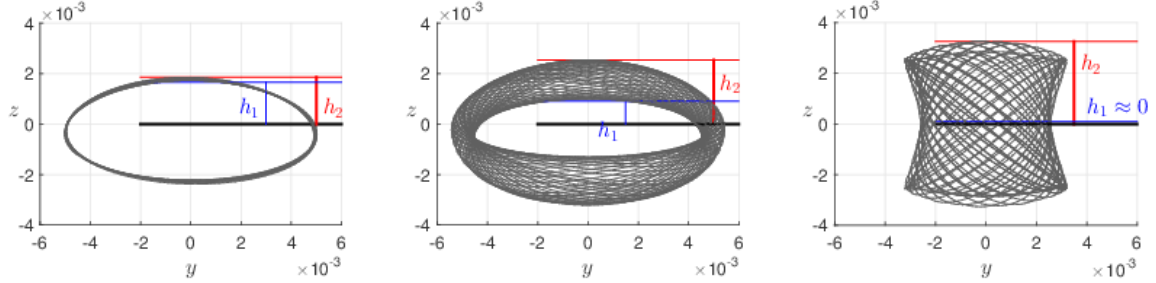

Figure 10: y-z projections of halo (left), quasihalo (middle), and Lissajous (right) orbits reached by the transfer orbits. The projections illustrate the definition of h_1, h_2, and the parameter $\lambda = h_1/h_2$ used to characterize the final LPOs.

Let h_1 and h_2 be the minimum and maximum (positive) z-amplitudes, measured from $z = 0$, of the y-z projection of the LPO, as shown in Fig. 10, we define the classifying parameter λ as h_1/h_2. Clearly, $\lambda \in (0, 1)$ for quasihalo orbits, and $\lambda \approx 0$ for Lissajous orbits. We can also label as halo orbits, those quasihalo orbits with $\lambda \approx 1$, although, as it has already been said, strictly speaking, in the 4-body model there are no periodic orbits. Orbits close to periodic planar and vertical Lyapunov orbits are classified as Lissajous (with very small z-amplitude and y-amplitude, respectively).
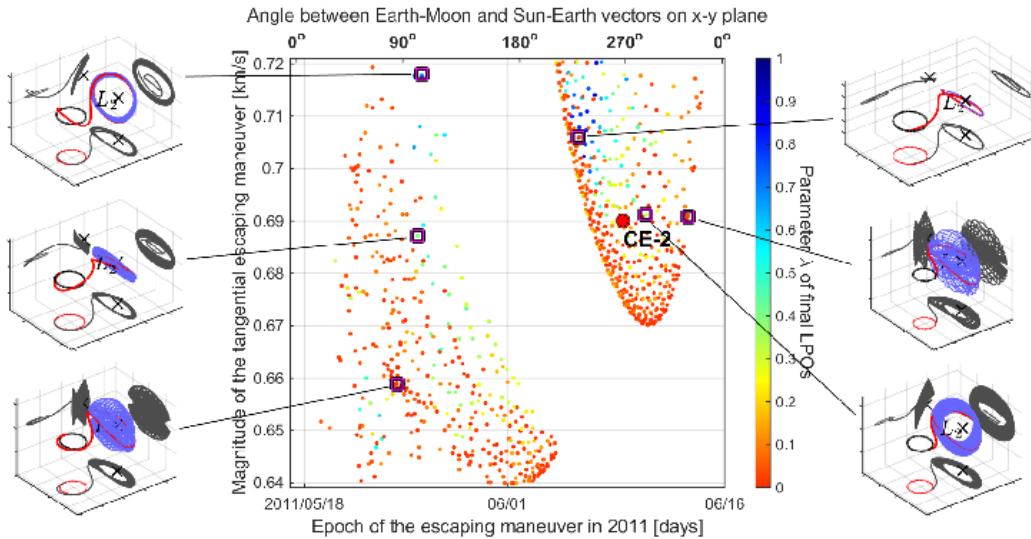
Figure 11: Classification of final LPOs, of the transfer trajectories shown in Fig. 9, according to the parameter λ.

The results obtained for the classification of the transfers of Fig. 9 according to the value of λ, are shown in Fig. 11. Due to the periodicity of the transfer pattern, these results can be translated to the transfer orbits determined for the one-year time of departure interval of

14

Fig. 6. Clearly, most of the LPOs are Lissajous and quasihalo orbits. The outer boundaries of the two families of transfers are all of Lissajous orbits, and the quasihalo orbits concentrate on the upper left corner. Halo orbits appear only in *Family II* and are associated with relatively large departure maneuvers Δv (above 700 m/s), Lissajous final orbits correspond always to the cheapest transfer opportunities of both families.

5   General epoch and orbital parameters at departure

The results shown for the CE2 analysis during the year 2011 are in fact very representative of the transfer possibilities we can obtain for any other particular year. In this section we analyze in more detail the impact of different orbital parameters of the departure lunar orbit on the transfer possibilities.

5.1   The semi-major axis and the departure epoch

We first consider a departure from a higher lunar orbit other than the one used by CE-2. In particular, we have considered a circular polar orbit around the Moon with an altitude of 600 km, this is, about 500 km higher than the one of CE-2, for the illustration of this section. All the other parameters remain unchanged. As one should expect, the results about the cost remain qualitative the same as in Fig. 5, distributed with the same periodic pattern as for the 100 km altitude departing orbit, but quantitatively shifted in terms of the value of the departing maneuver Δv. Basically, the difference is of the order of 77 m/s, which agrees very well with the difference between the lunar escape speeds from the two departure orbits. This gives us a Δv range of [560 m/s, 640m/s], as it can be seen in Fig. 12 where only direct transfer trajectories with a time of flight less than 45 days are represented. This simple fact on the value of the departure maneuver can be considered a general rule of thumb when the semi-major axis of the lunar orbit is changed.
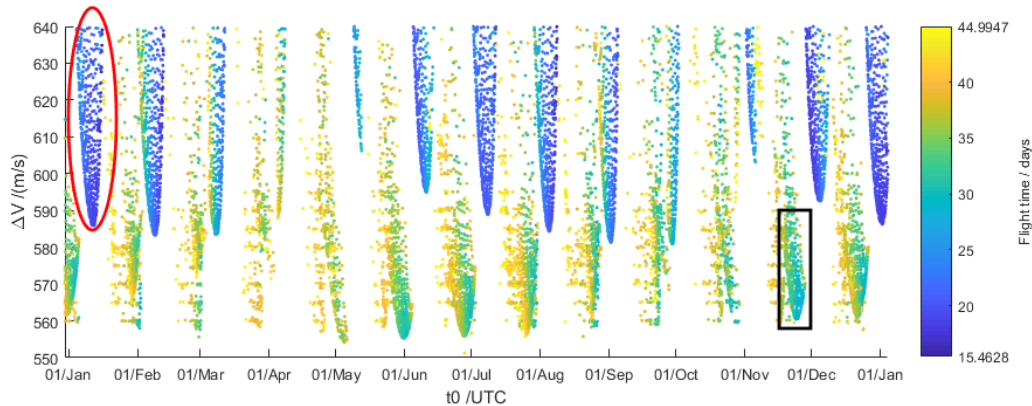

Figure 12: Time of flight (days) and Δv (m/s), as a function of the departing epoch during the year 2011, of the transfer trajectories with a time of flight less than 45 days. The inclination of the departing lunar orbit is 83.9^o and its altitude 600 km. We consider the transfers sets marked with a rectangle (set I in *Family I*) and with an ellipse (set II in *Family II*).

For this higher altitude orbit we have analized the role of the departure epoch. Inside

the two families of transfer trajectories, we have considered two main sets for a more detailed analysis. They are the ones marked by a rectangle (set I in *Family I*) and by an ellipse (set II in *Family II*) in Fig. 12, moreover, we extended the maximum value Δv_{max} to 700 m/s for the orbits in set II. A magnification of both sets is shown in Fig. 13.
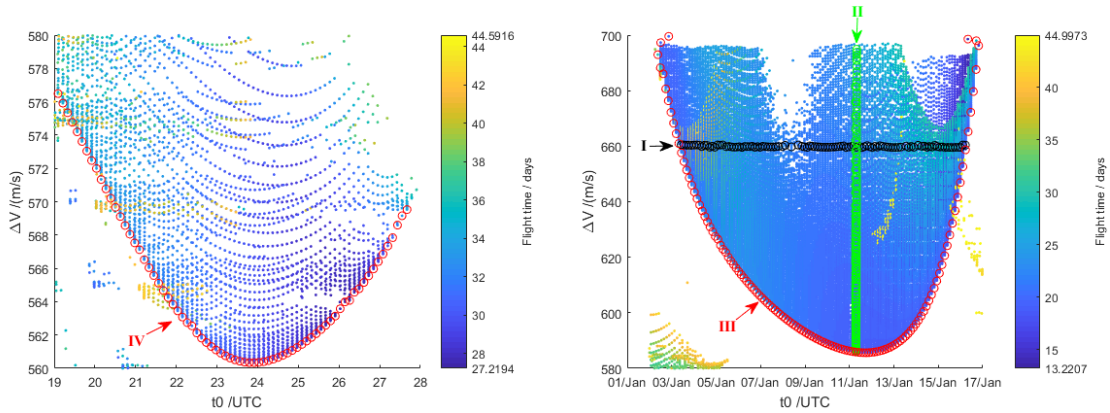

Figure 13: Samplings inside sets I (left) and II (right).

In order to describe the results of this analysis, we consider a few sets of orbits in both regions; these are those with almost the same initial transfer maneuver and different departing epoch (sample I, black line in Fig. 13), those departing at almost the same epoch with different initial transfer maneuver (sample II, green line), and the boundaries of sets I and II (sample III in Fig. 13 (right), and IV in Fig. 13 (left), both in red). It is worth to remark that sample II orbits are not along a straight line as it might seem, but along the curve shown in Fig. 14. All the transfer trajectories along this curve have slightly different departure time, but all them are along the same revolution of the lunar orbit. The much longer time scale used in Fig. 13 squeezes this curve into a line. Furthermore, it should be remarked that both sets I and II, are composed by such curves (each one associated to the same revolution of the lunar orbit), implying that the phase on lunar orbit also plays a main role in the geometry of both regions.
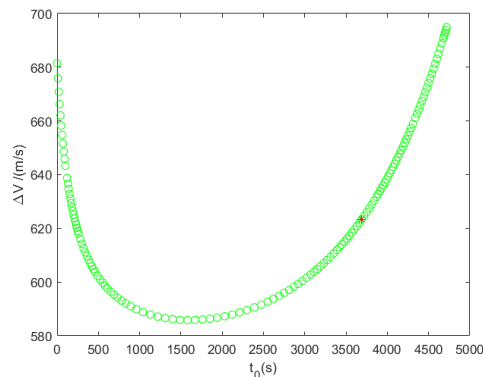

Figure 14: Sample II inside set II in Fig. 13 taking departing epochs between t_0 and $t_0+5000 \, s$ (in seconds), with t_0 fixed at 12:35:01, Jan 11, 2011. All the transfer orbits represented on this curve are along the same revolution of the departing lunar orbit.

16

Figs. 15 and 16 show the results obtained for the four samples of transfer orbits. We have used the Jacobi constant of the Sun-Earth restricted three-body problem as an indicator of the final LPO energy. This energy value, together with the y and z amplitudes, as well as the $\lambda \in (0, 1)$ index used for the classification of the libration orbits, are the parameters displayed in this figure. For all the samples, the LPO energy decreases as the amplitudes increase, or vice versa, which is accordance with the results in [13].

From these figures follow some interesting results. For transfers of sample I, the overall trend of the LPO amplitudes appears to increase with the index N used to parameterize the curves (red, black and green) shown in Fig. 13,. Since this index can be associated to the departure time, it indicates that, with the same velocity increment, the LPO amplitudes generally increase as the departure time is postponed for the transfer trajectories of set II. Meanwhile, and according to the value of λ, the corresponding LPOs include the quasi-halo orbits and Lissajous orbits (i.e., a LPO with λ less than 1 is a Lissajous orbit, otherwise it is a quasi-halo one). In order to illustrate these results, seven samplings, marked with a boxed number in Figs. 15 and 16, are shown in Fig. 17. For transfers inside sample II, again the reached LPOs include both quasi-halo and Lissajous orbits when departing from the same lunar revolution.

Finally, for samples III and IV, that are the boundaries of sets I and II corresponding to transfer trajectories with minimal velocity increment, all the arrival orbits are Lissajous, most of them have a y-amplitude larger than the z-amplitude (the ratio between both amplitudes varies in a range from 2.5 to 3.5).

5.2   Inclination and longitude of ascending node

Although near polar orbits are the natural nominal candidates for most of the lunar orbiting missions, it is also interesting to consider transfers to LPO departing from other inclinations. The impact of the longitude of the ascending node Ω it is also worth to be studied while the influence of ω is negligible for almost circular orbits. For all these general explorations in this section, we are going to consider the inclination and the longitude of the ascending node of the lunar departure orbit measured with respect to the ecliptic plane, since they seem to be more natural to analyze these kind of transfers. However it is worth to mention that the same analysis of this section considering the J2000 equatorial reference present minimal differences in the results. The conversion of the orbital elements i and Ω from the J2000 equatorial values of CE-2 given in Table 1 into ecliptic ones give 87.91° and 260.26° respectively. From now on, and otherwise stated, the nominal ecliptic values considered will be $i = 88°$ and $\Omega = 260°$. For a given pair (i, Ω) in ecliptic coordinates, the initial conditions defining a departure in this section are obtained converting this pair into J2000 equatorial and completing the set of orbital elements and epoch with the remaining values of CE-2 given in Table 1.

We have started exploring the transfers associated to departures from lunar orbits with inclinations close to the one of CE-2, considering ecliptic inclinations varying from $i = 68°$ to 108° with a step of 5°. Again, we have only considered direct transfers with a time of flight less than 43 days, as in the bottom line of Fig. 6. The results obtained are shown in Fig. 18. As in previous figures, the lower x-axis displays the departure epoch t_d, and the upper x-axis the phase angle θ of the Sun-Earth-Moon geometry at departure. The label at the right side of each plot indicates the inclination of the departing lunar orbit.

As it is clear from Fig. 18, the results do not vary too much with the inclination, and are
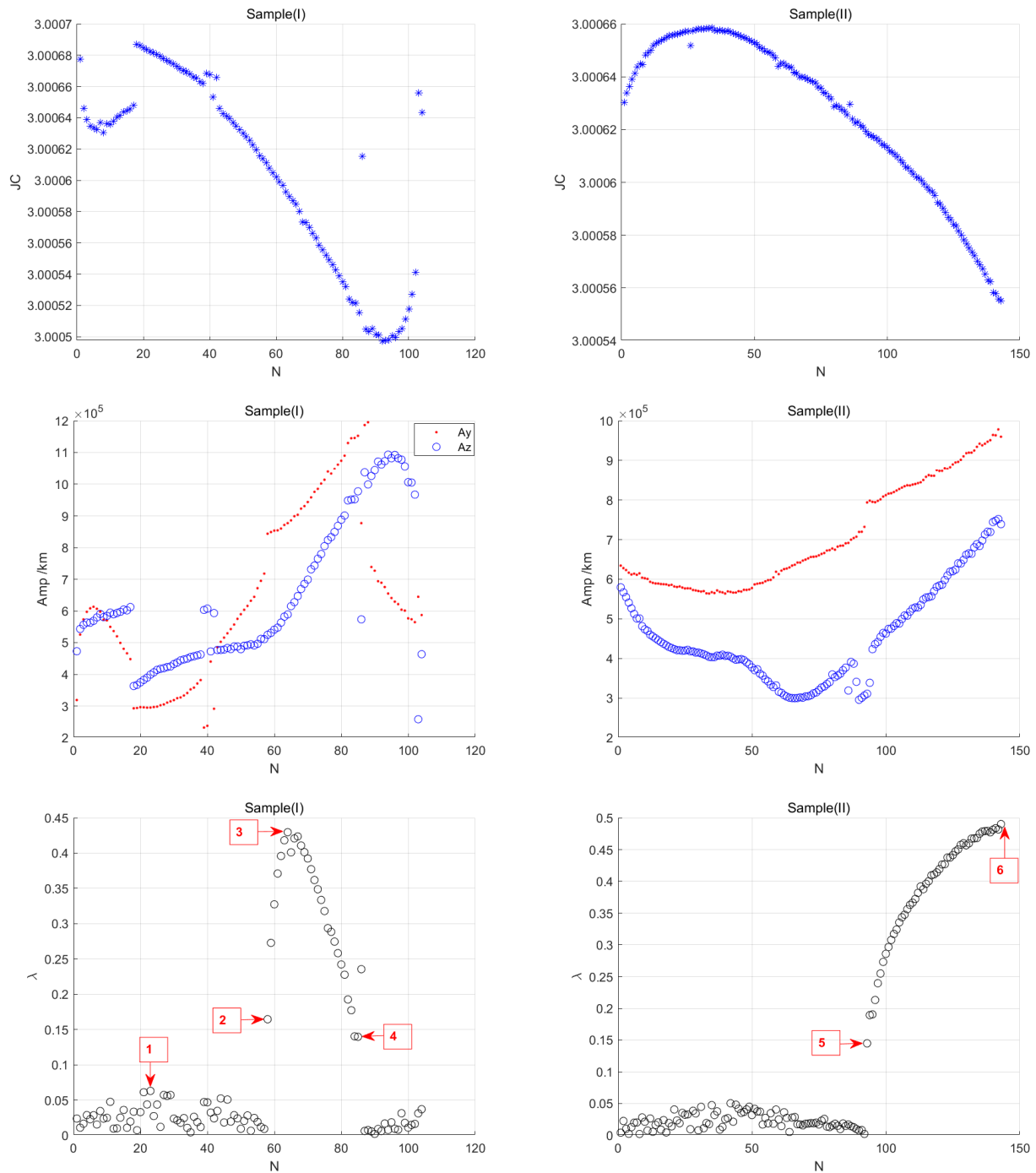
17

Figure 15: Characteristics (Jacobi constant, y and z-amplitudes, and λ) of the orbits of the sampling sets I and II of Fig. 13. The orbits of these sets have been parametrised by a sample number $N \in [0, N_{max}]$, where N_{max} is the total number of orbits computed in each set. The orbits with labels 1, 2, 3, 4, 5 and 6 are displayed in Fig. 17.
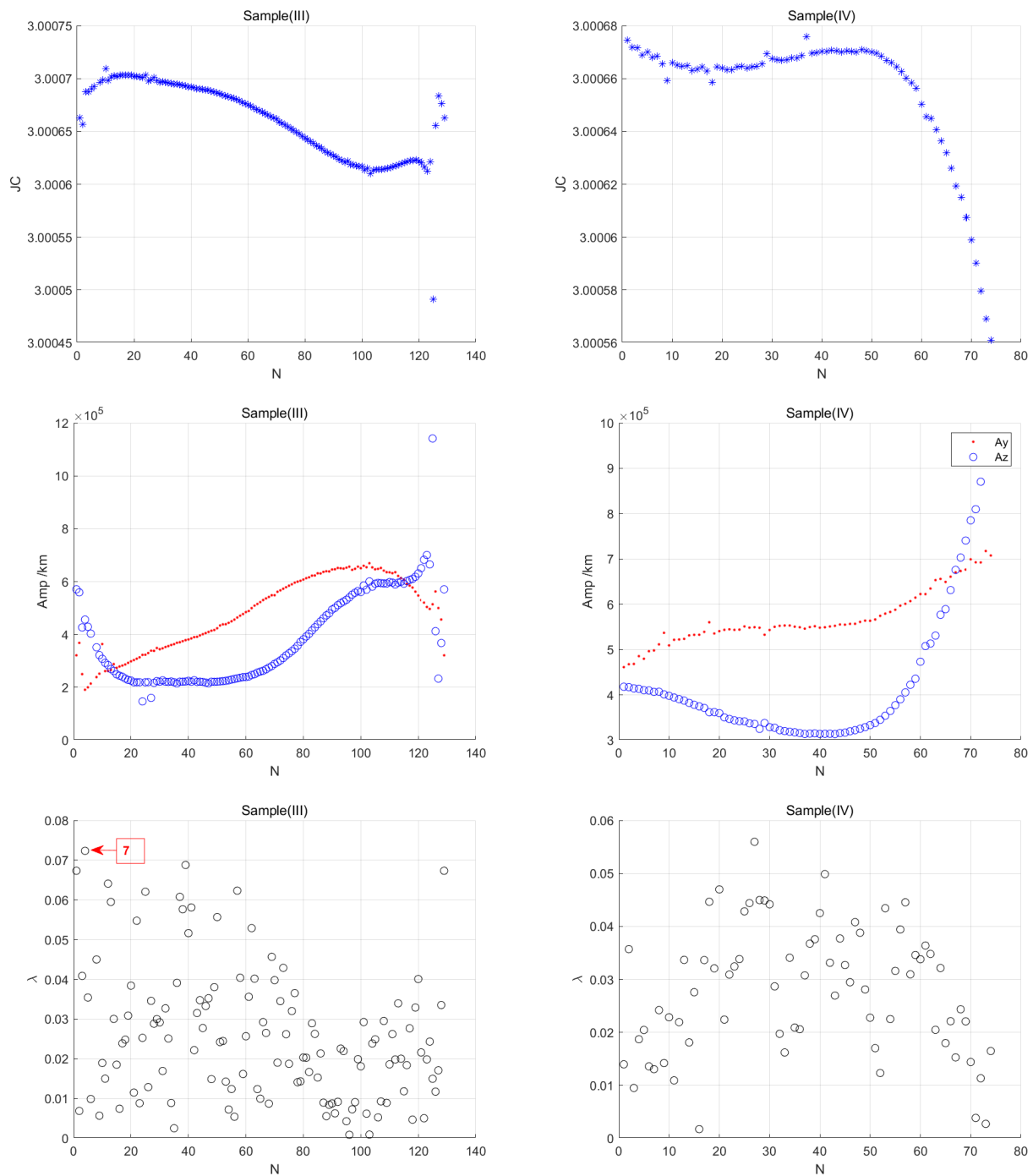
18

Figure 16: Same as Fig. 15 for the orbits of the sampling sets III, and IV of Fig. 13. The orbit with label 7 is displayed in Fig. 17.

Orbit 1 of sample I

Orbit 2 of sample I

Orbit 3 of sample I

Orbit 4 of sample I

Orbit 5 of sample II

Orbit 6 of sample II

Orbit 7 of sample III
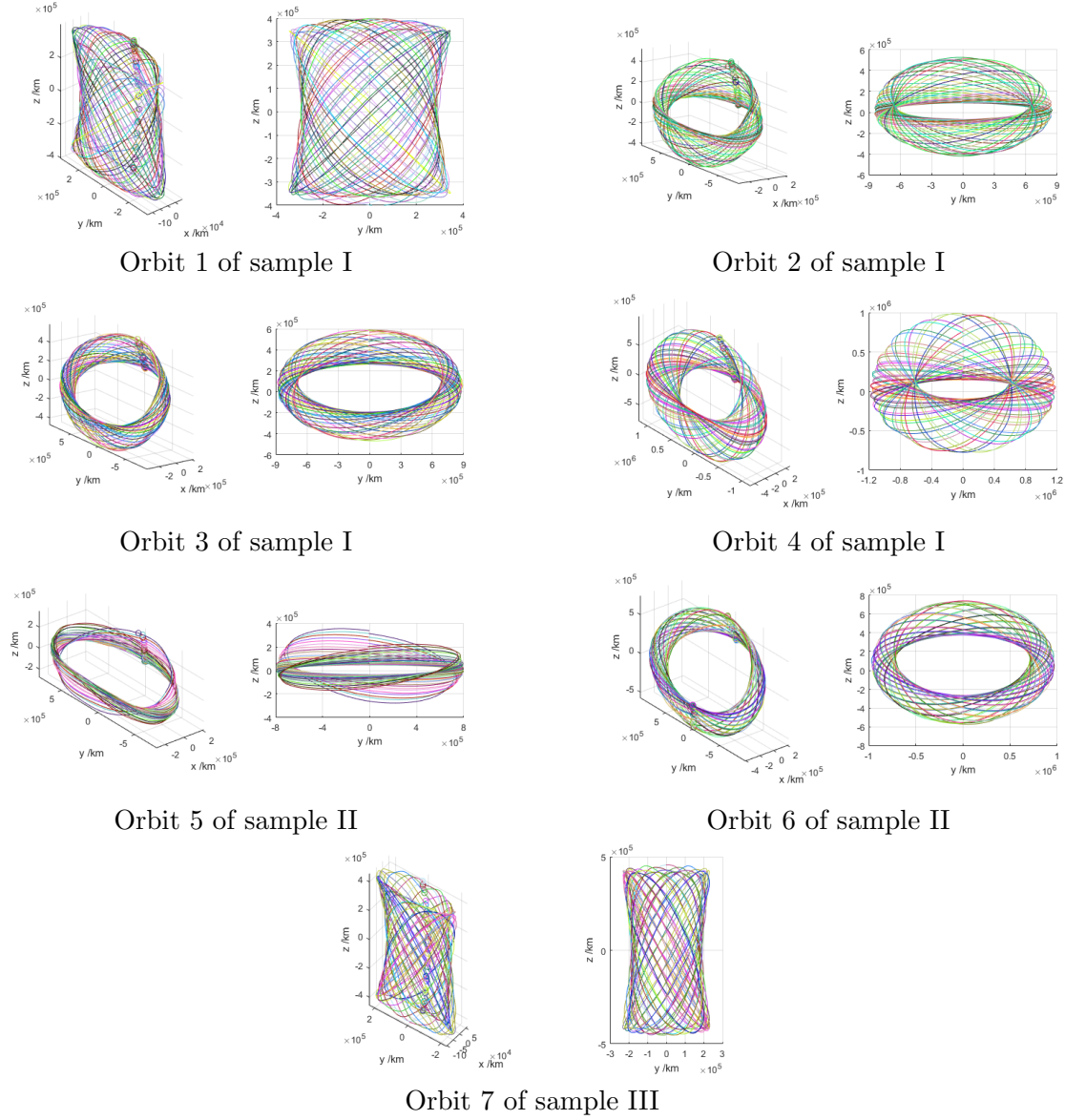
Figure 17: Some orbits in (x, y, z) synodical coordinates, of the sets I and II, corresponding to the four sampling sets shown in Figs. 15 and 16. From top to bottom and left to right, the orbits correspond to the seven boxed numbered orbits these figures.

similar to the ones obtained for $i = 88°$ with the same maximum time of flight. Again, for all the inclinations we find two families of direct transfers, *Family I* and *Family II*, with a pattern that repeats, approximately, every month. In *Family I* there are the transfers that require less initial Δv; *Family II* has a more clear boundary than *Family I*, although if the maximum allowed time of flight were increased, then the boundary of this family would also become fuzzy. In northern hemisphere winter and summer months, these two families appear more robust when the initial inclination i varies. *Family II* moves upward as i increases, which

means that ΔV increases. The time of flight t_{FT} required by the orbits of both families to reach the LPO region almost does not change with respect to the inclination. In spring and autumn months, both families do not change too much when i increases from 88° to 108°, but when it decreases from $i = 88°$, *Family I* shrinks to the bottom of the plot and *Family II* shows new branches with transfer orbits requiring less t_{FT}. Some of these new branches also appear in May and November, as it can be seen in the two upper plots with $i = 103°$ and 108°.

From the point of view of choosing a wider and steadier launch opportunity, the selection done for the CE-2 mission seems appropriate. In Fig. 19, the CE-2 transfer is represented by a small red point located near the center of the *Family II* in June of the $i = 88°$ slice. Its location is not sensitive either to a small error in t_d, nor to an error of the instantaneous inclination i. Nevertheless, it is worth to note that *Family I* also has a dense region showing a steadiness similar to the one of *Family II*, so transfer orbits of this family could be also potential alternative transfers, with lower ΔV but with a slightly larger value of t_{TF}.

In a second step we have explored the behavior varying the ecliptic inclination in the whole range from 0° to 180°. The result is displayed in Fig 20. The most important point is that for low inclinations the pattern of *Family II* becomes more steady loosing the remarked apparent seasonal dependence that one finds attached to the near polar orbits, moreover the smallest local minimum Δv values inside this family are attained when $i = 0°$. The monthly pattern regularity in *Family II* is also observed for inclinations near 180°, although in this case the local Δv minima in the family is the highest one due to the retrograde motion. As for *Family I*, the monthly regularity of the pattern becomes quite clear for all inclinations, although for $i = 90°$ is when the range in Δv is more uniformly covered.

In Fig. 21 we show the results of the exploration with respect to the ascending node. Values in Ω ranging from 0° to 330° with a step of 30° are presented always for an ecliptic polar orbit ($i = 90°$), where the apparent seasonal dependence of *Family II* is more evident as it has been mentioned in the discussion of Fig. 20. The results clearly indicate that this monthly dependence is not seasonal but in fact it is attached to the value of the ascending node.

The shifting periodic behavior with respect to Ω observed in Fig. 21 for $i = 90°$ is similar when taking any of the inclination plots of Fig. 20, and the combination of both figures provides a clear indication of the result one should obtain for an arbitrary pair (i, Ω). Finally, in Fig. 22 we put together in the same plot all the results obtained for the simulations shown in Fig. 20, varying the inclination, and in Fig. 21, varying the ascending node, providing a clear view on how the *Families I* and *II* distribute over the year. The bottom subplot of this figure is enlarged in Fig. 23 including a sine plot of the angle θ defined in Fig. 8 (conveniently shifted and scaled). It is clear that *Family I* is attached and centered in the neighborhood of $\theta = 90°$ (third quarter Moon) and *Family II* about $\theta = 270°$ (first quarter Moon) while the transitions are associated with the collinear configurations $\theta = 0°$ and $\theta = 180°$ (full and new Moons respectively). We notice also that a somewhat less dense set of transfer opportunities happens about the full Moon transition.

5.3 Transfer opportunities covering Saros and Metonic periods

Up to this point, the analysis has been performed for transfer orbits during the year 2011 in order to compare with the CE-2 mission reference while in this section, the transfer opportu-
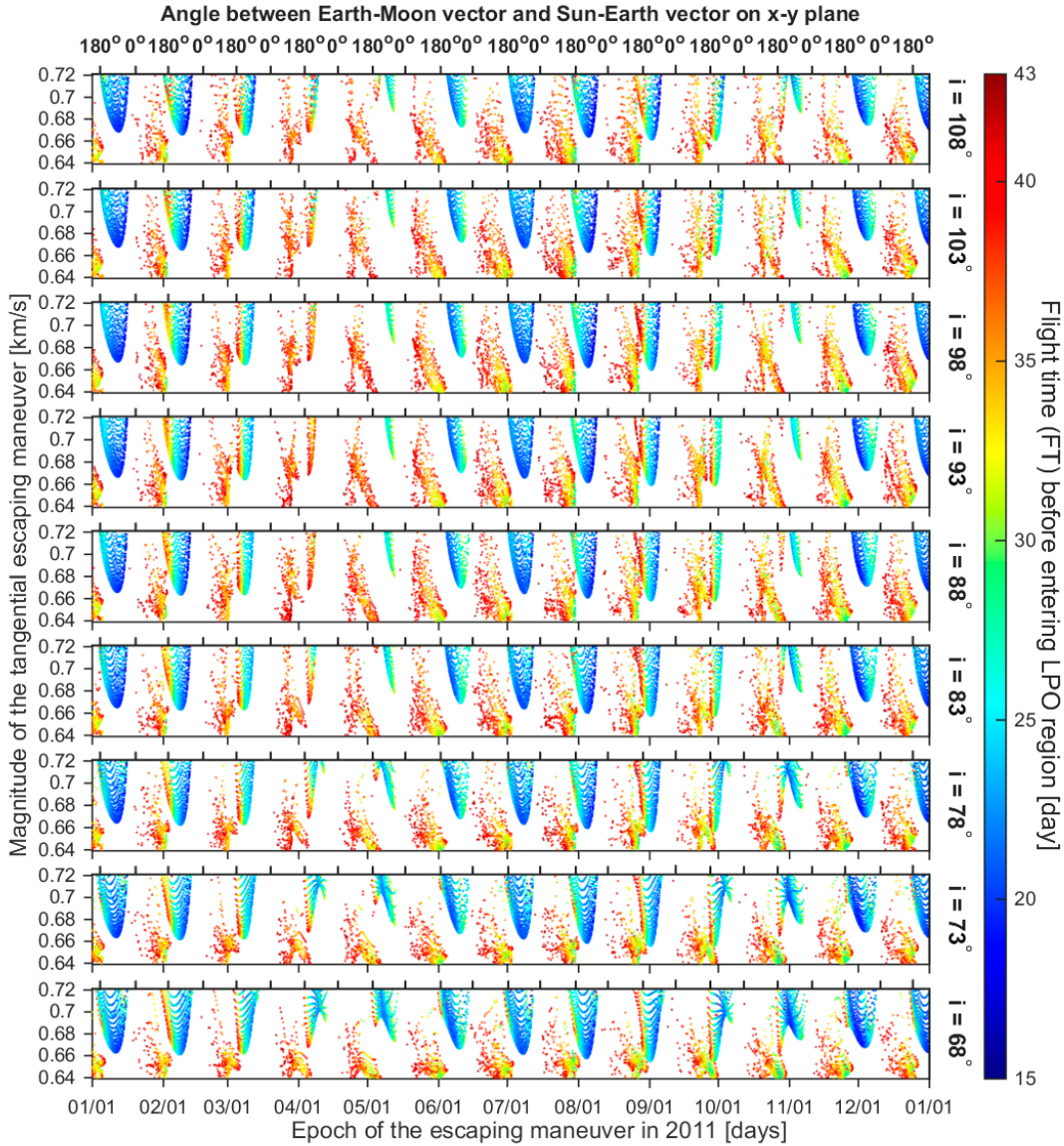
Figure 18: Behavior of the transfer opportunities with $t_{\mathrm{FT}} < 43$ days represented by means of the magnitude of initial departing maneuver Δv and the departure epoch t_{d}. The inclination of the initial lunar orbit, measured with respect to the ecliptic, varies from $68°$ to $108°$ with a step of $5°$ about the one of CE-2 ($i = 88°$). For all plots the longitude of the ascending node of the departure lunar orbit with respect to the ecliptic is $\Omega = 260°$.

nities have been analyzed for a time interval of 20 years. Since the length of the month in the Gregorian calendar and the synodic lunar period do not agree, one can expect a yearly shift of the transfer families shown in Fig. 18. The explorations confirm that the main behaviors continue, but a slight yearly shift of the families appears, closing a cycle with a period of 19 years. This is, coinciding with the Metonic cycle, which it is almost one year larger than the
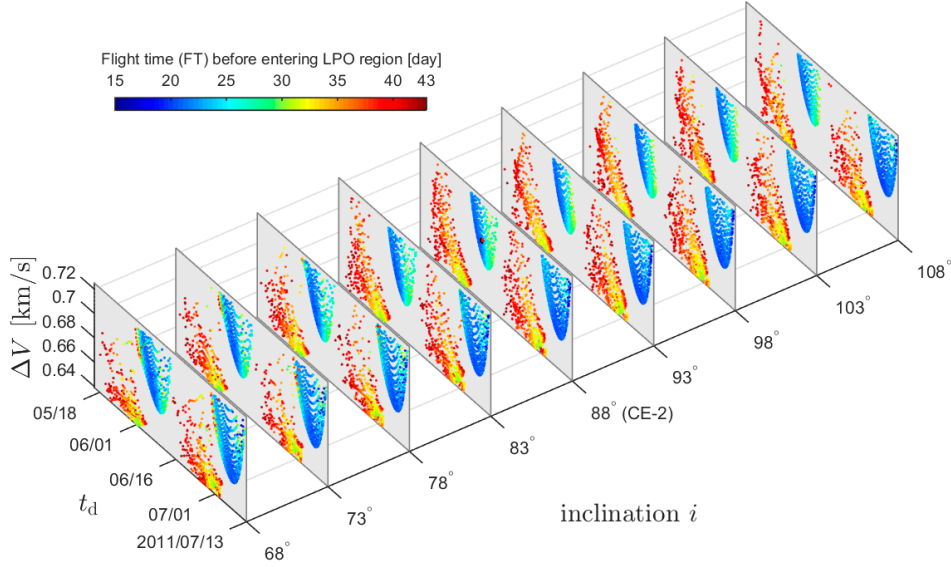
Figure 19: Enlargement of Fig. 18 showing a two-month time interval around the initial transfer condition of CE-2 (displayed with a small red dot in the $i = 88°$ slice). Clearly, the region covered by the transfer orbits of *Family I* contracts as i decreases.

Saros period. We recall that the Metonic cycle is a 19-year period after which is nearly a common multiple of the tropical year ($\sim$365.2422 days) and the synodic lunar month ($\sim$29.53 days) and, as a consequence, after 235 lunations, the lunar phases repeat on the same day of the year. Furthermore, this 19-year period is also close to the period of the precession of the Moon ($\sim$18.59 years).

To illustrate the behavior, we consider the same orbital parameters of CE-2 given in Table 1 but varying the departure epoch. The results are shown in Fig. 24 from the year 2011 (coincident with $i = 88°$ in Fig. 18) up to the year 2030. From the figure it follows that, leaving aside the slight shift due to the fact that the length of the month is not coincident with the synodic lunar period, the average pattern for the different families of transfers is kept from one year to the next one. In particular, the seasonal dependence of the concentration of transfer opportunities in *Family II* (during the northern hemisphere winter and summer months of the plot) experienced for near polar orbits, persists. This fact corroborates again that their location over the year depends only on the value of the ascending node as it was illustrated in Fig. 21.

As it can be seen in Fig. 24, the pattern distribution across the years follows a periodic behavior, corroborated also by the change of density in *Family I* during April and October (even that in terms of Δv cost or time of flight they remain always in the same bounds), and finally, the subplots of transfer opportunities of 2011 and 2030 (after 19 years) almost coincide. In Fig. 25, we compare the transfer opportunities for these two years. The top subplots of the figure are a copy of the ones of 2011 and 2030, while the bottom one is the overlapping of them, clearly showing their almost coincidence.
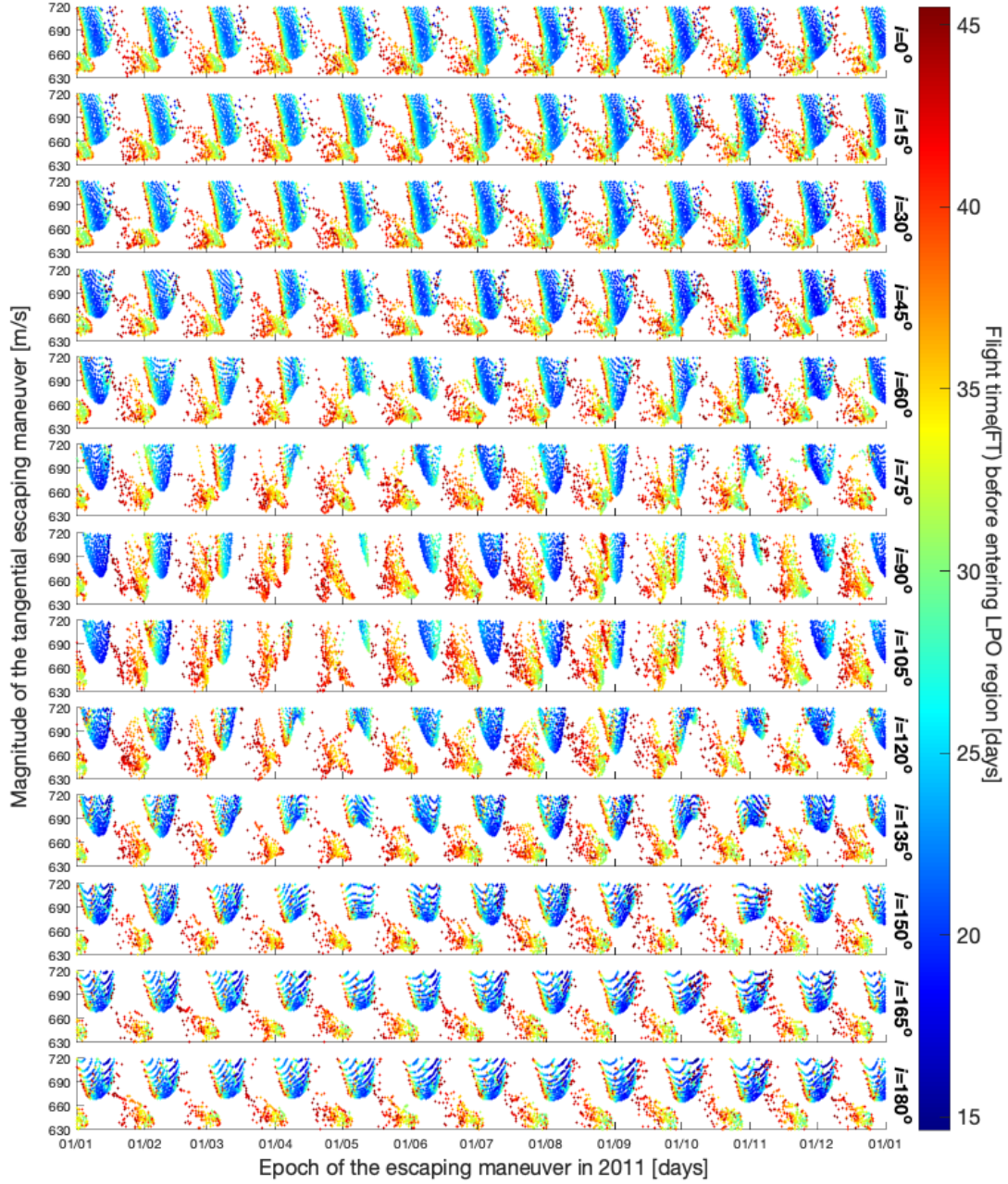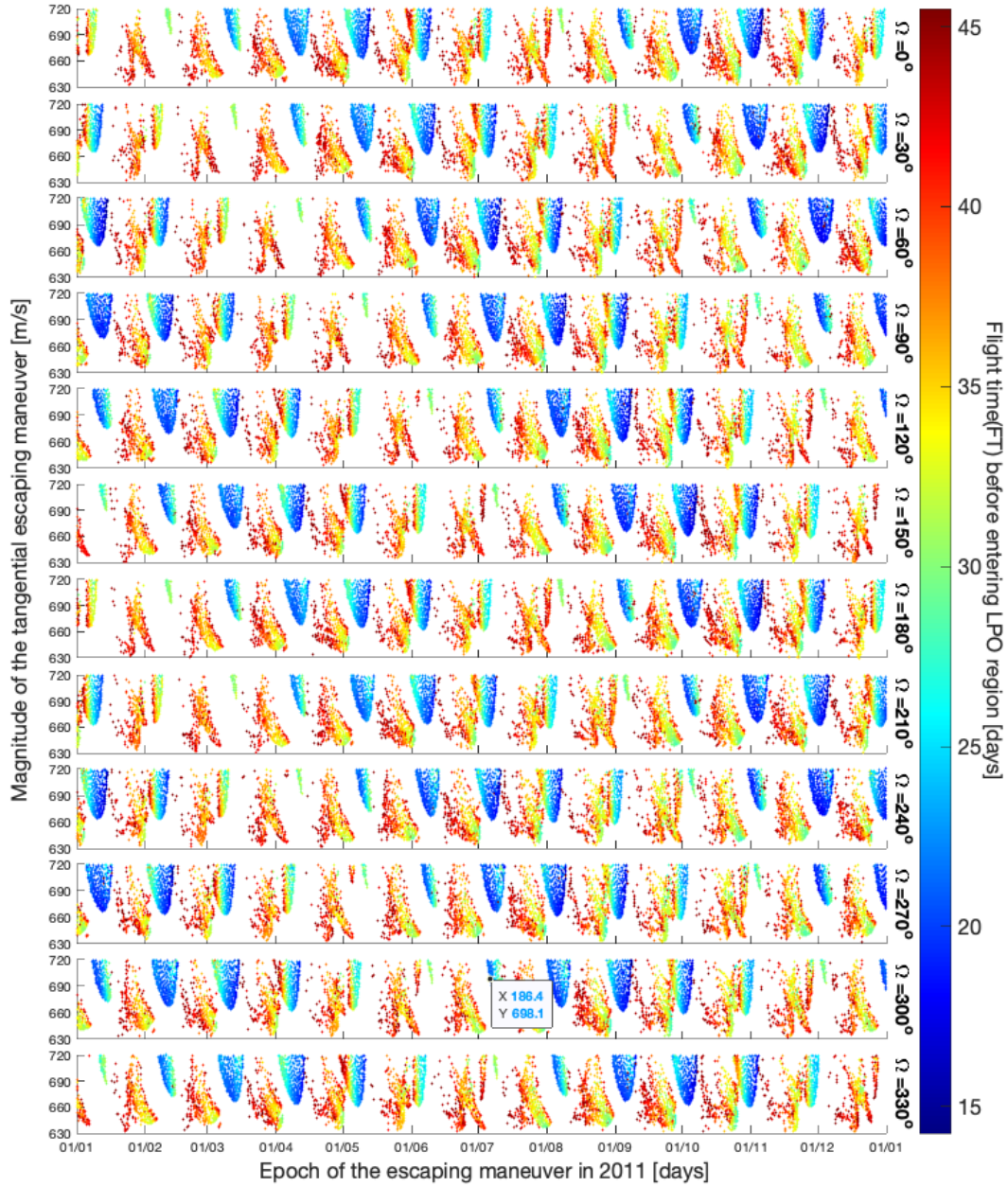
23

Figure 20: Behavior of the transfer opportunities with $t_{\mathrm{FT}} < 43$ days represented by means of the magnitude of initial departing maneuver Δv and the departure epoch t_{d}. The ecliptic inclination of the departure lunar orbit varies from $0°$ to $180°$ with a step of $30°$ while the value of the ecliptic ascending node is kept fixed to $\Omega = 260°$.

Figure 21: Behavior of the transfer opportunities with $t_{\mathrm{FT}} < 43$ days represented by means of the magnitude of initial departing maneuver Δv and the departure epoch t_{d}. The longitude of the ascending node of the departure lunar orbit in the ecliptic plane varies from $0°$ to $330°$ with a step of $30°$, while the value of the ecliptic inclination is kept fixed to $i = 90°$.
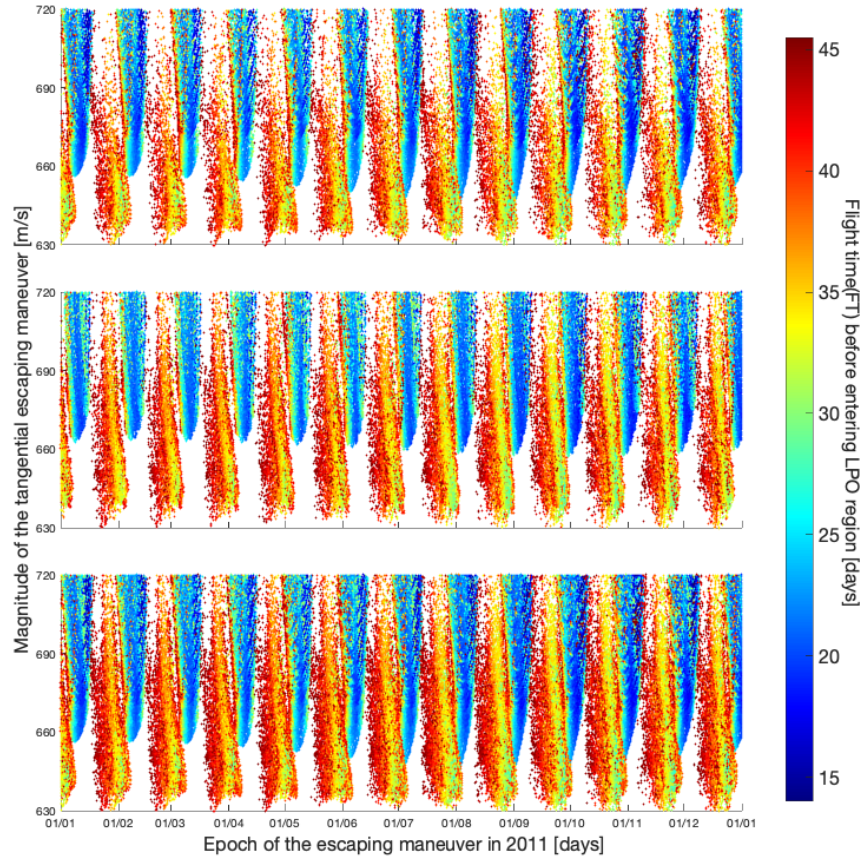
Figure 22: Overlapping of the results obtained in the simulations of Figs. 20 and 21. In the top row we show the overlapping with respect to the inclinations, in the middle one the overlapping with respect to the ascending node, while in the bottom row we include both.
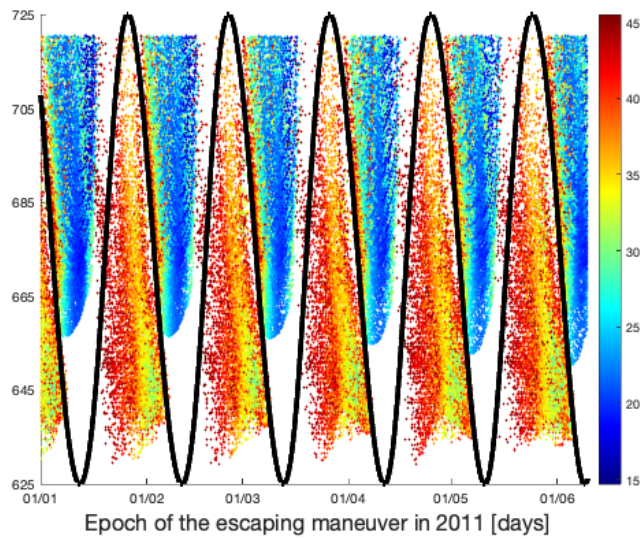
Figure 23: Detail of the bottom subplot of Fig. 22 including a conveniently scaled and shifted sine plot of the Sun-Earth-Moon configuration angle θ defined in Fig. 8
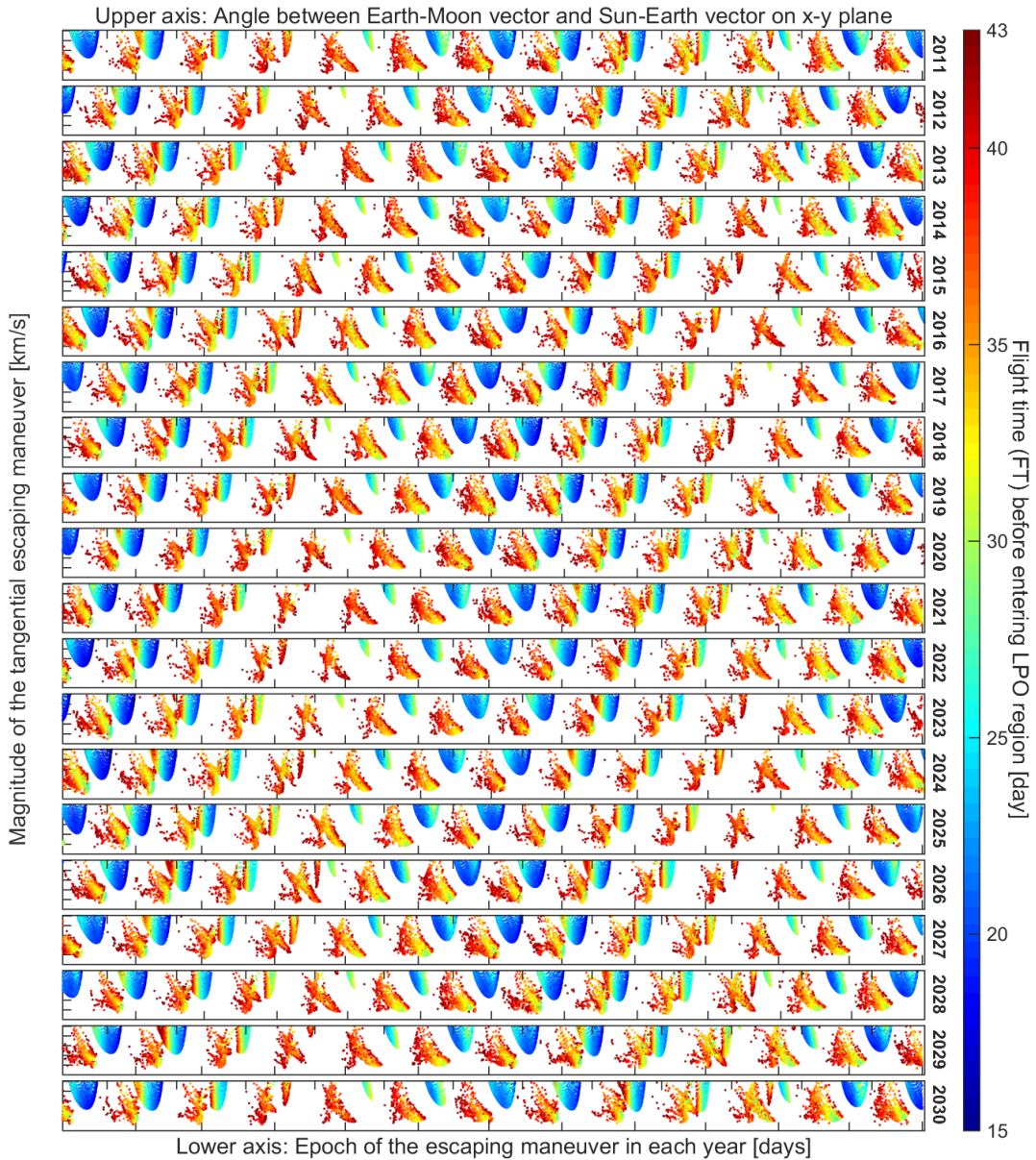
Figure 24: Transfer opportunities departing with the same orbital elements as CE-2 but extending the departure epoch from 2011 to 2030. The year is provided on the right side of each plot. The x-axis ticks on the top give the phase angle θ between the Earth-Moon and the Sun-Earth directions at departure, and two consecutive ticks are separated by $360°$. The ticks in the lower axis correspond to the departure epoch and marking the first day of each month of the year, always starting on January first. The numbers in the axis have been omitted.
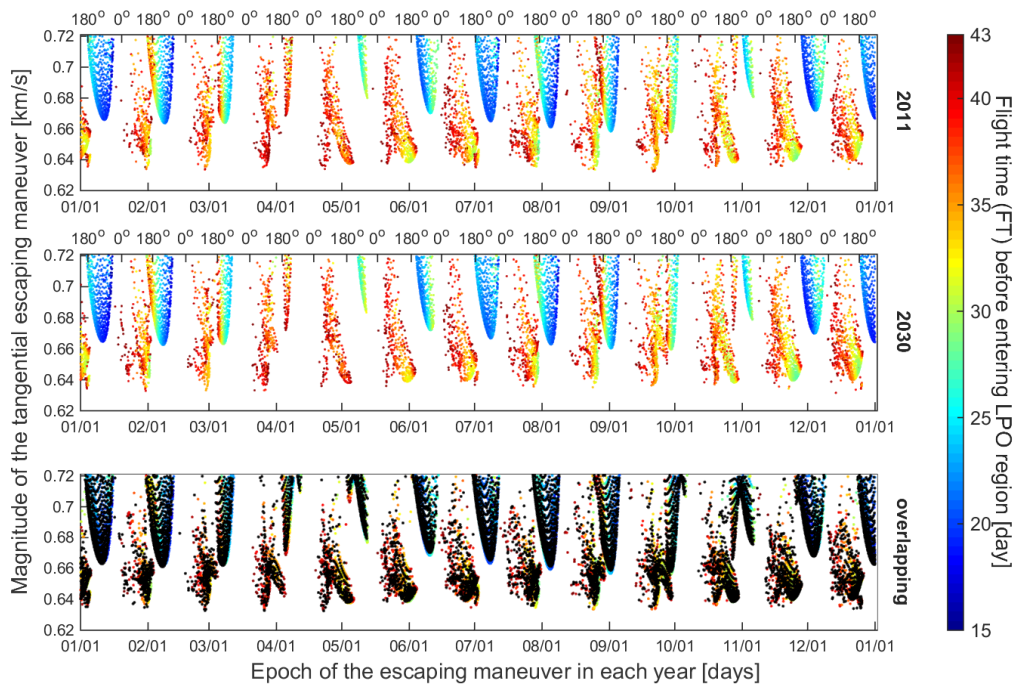
Figure 25: Comparison between the transfer opportunities in 2011 and 2030. The bottom plot is the overlapping of both, where the black dots correspond to the year 2030 and the other ones to 2011.

6   Preliminary study of the TCM1

In this section we address the so called first trajectory correction maneuver (TCM1), that is the one responsible for the correction of the errors introduced in the execution of the initial departure maneuver, Δv, due to the inaccuracies of the thruster. The analysis follows a similar approach to the one in [11] for the transfer from a parking orbit around the Earth to a LPO around the equilibrium point L_2 of the Sun–Earth system, ignoring navigation errors. Contrary to other more general approaches for TCMs, like the ones of Qi & de Ruiter [28], focusing in tracking a previous defined transfer trajectory, the approach we follow focuses in the determination of a new LPO target orbit, which someway measures the sensitivity of the transfer problem in terms of the variation of the final LPO orbit with respect to an injection error.

6.1   Injection errors

For the determination of the TCM1, we assume two different kinds of errors in the velocity of the spacecraft after the execution of the departure maneuver Δv. If $\boldsymbol{V}_{\mathrm{d}}^{\mathrm{ref}} \in \mathbb{R}^3$ denotes the nominal velocity along the reference transfer orbit at departure while $\boldsymbol{V}_{\mathrm{d}} \in \mathbb{R}^3$ denotes the actual velocity, we are going to study the impact of and error affecting only the modulus of $\boldsymbol{V}_{\mathrm{d}}^{\mathrm{ref}}$, or affecting its direction. In the first case we can write

$$\boldsymbol{V}_{\mathrm{d}} = \boldsymbol{V}_{\mathrm{d}}^{\mathrm{ref}} \left(1 + \varepsilon/\|\boldsymbol{V}_{\mathrm{d}}^{\mathrm{ref}}\|\right) = \boldsymbol{V}_{\mathrm{d}}^{\mathrm{ref}} + \Delta \boldsymbol{V}_{\mathrm{d}}. \tag{4}$$

According to [32], one can assume a maximum injection error of the order of 1.15 m/s, and for the present paper, we have taken $\varepsilon \in [-1.15, 1.15]$ m/s. In the second situation one can write the final velocity as

$$\boldsymbol{V}_{\mathrm{d}} = \boldsymbol{V}_{\mathrm{d}}^{\mathrm{ref}} + \Delta \boldsymbol{V}_{\mathrm{d}}, \tag{5}$$

where $\Delta \boldsymbol{V}_{\mathrm{d}} \in \mathbb{R}^3$. In this case we have assumed that $\Delta \boldsymbol{V}_{\mathrm{d}}$ follows a normal distribution with $3\sigma_1 = 1.15$ m/s along the tangential direction and with $3\sigma_2 = 0.15$ m/s along the cross-track direction.

6.2   Strategy and parameters for the computation of the TCM

The strategy used for the computation of the TCM is based on the determination of a new LPO, as target final orbit, instead of tracking a previously defined reference transfer trajectory. The computation of the TCM, denoted by $\Delta \boldsymbol{V}_{\mathrm{TCM}}$, is illustrated in Fig. 26. Due to the injection error $\Delta \boldsymbol{V}_{\mathrm{d}}$, the trajectory deviates from the nominal one, and once detected, at $t = t_{\mathrm{d}} + t_{\mathrm{TCM}}$, a trajectory correction maneuver $\Delta \boldsymbol{V}_{\mathrm{TCM}}$ is planned and executed to target the spacecraft to a final new LPO, close to the original one.

The bisection procedure, explained in Section 3.2, provides a well-established way to reconstruct a new transfer trajectory starting from the deviated state at epoch t_{TCM}. Here t_{TCM} is counted (in days) from the starting epoch t_d. If the injection errors are small, the deviation at t_{TCM} should also be small and, the bisection method easily converges to a suitable new solution.

The maneuver $\Delta \boldsymbol{V}_{\mathrm{TCM}}$ is represented by a three-dimensional vector in the body-centered velocity frame displayed in Fig. 3, so its direction is defined by two angles $\alpha \in [-180°, 180°)$
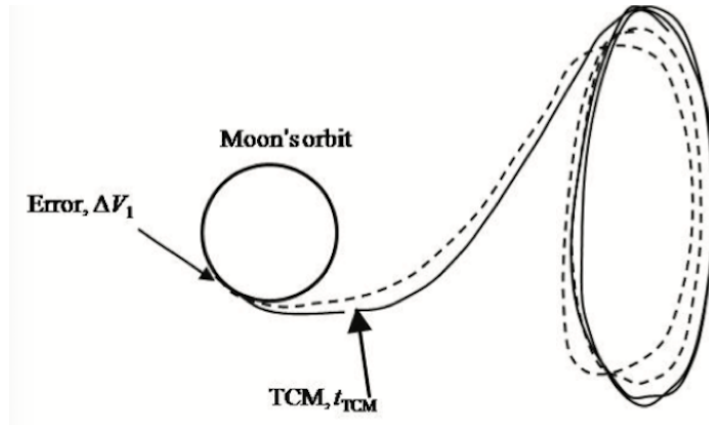
Figure 26: Illustration of the strategy followed for the computation of $\Delta \boldsymbol{V}_{\text{TCM}}$. The dashed line represents the initial nominal transfer trajectory and the final LPO. The solid line represents the reconstructed transfer trajectory to a new final LPO.

and $\beta \in [-90°, 90°]$. Taking into account that (α, β) and $(-\alpha + 180°, -\beta)$ give two collinear but reversed directions, in the bisection procedure both $\pm \delta v$ are explored at the same time and we can reduce the exploration to the half sphere: $\alpha \in [-90°, 90°]$, $\beta \in [-90°, 90°]$.

Denoting by ΔV_{TCM} the modulus of the TCM along the direction specified by the angles $(\alpha_{\text{TCM}}, \beta_{\text{TCM}})$, A_z^* the z-amplitude of the new LPO, and λ^* the parameter characterizing the new LPO, we have a relation between these variables that can be written as

$$(\Delta V_{\text{TCM}}, A_z^*, \lambda^*) = \mathcal{F}(\Delta \boldsymbol{V}_{\text{d}}, t_{\text{TCM}}, \alpha_{\text{TCM}}, \beta_{\text{TCM}}). \tag{6}$$
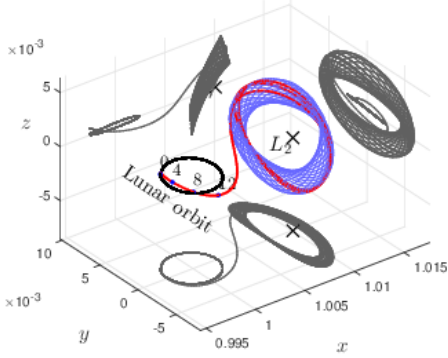
6.3 Reference transfer trajectories

For the TCM computation, we have used two different transfer trajectories as reference paths, one in each of the two families discussed in Fig. 6. For the transfer orbit of *Family II*, we have chosen a trajectory with the initial condition close to the one of CE-2, and is displayed in Fig. 27b. For *Family I* we have used a transfer orbit whose shape, as well as the one of the final LPO, is similar to the one of *Family II*, as is shown in Fig. 27a. Nevertheless, it must be noted, looking at the position of the spacecraft after 0, 4, 8 and 12 days (displayed and labeled in both figures), that the transfer orbit of *Family II* is faster than the one of *Family I* (21.79 days vs 35.44 days) although it requires a larger initial ΔV (0.68955km/s vs 0.66752 km/s).

## 6.4 TCM for tangential velocity errors

We first consider the case where the error only affects the modulus of the injection maneuver and, according to Eq. 4, we denote by ε the magnitude of the tangential error. Studying the relation between ΔV_{TCM} and the angles α_{TCM}, β_{TCM} it will be shown that, for a given ε and a certain t_{TCM}, one can find a local optimum $\Delta \boldsymbol{V}_{\text{TCM}}^*$ leading the spacecraft to a new, but similar, LPO.

31
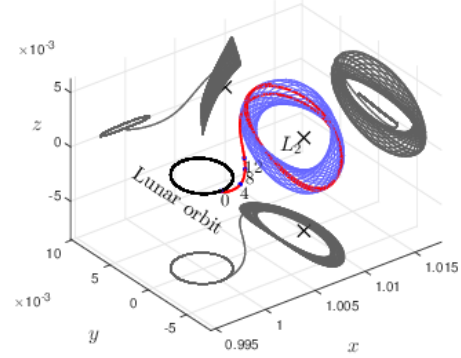
(a) Direct transfer in *Family I*   (b) Direct transfer in *Family II*

Figure 27: Reference transfer trajectories of the two families of transfer orbits that are used for the TCM analysis. The transfer orbit of *Family II* is close to the one used by CE-2, as well as the final quasihalo LPO reached by the spacecraft (see [22]).

6.4.1   Local optimal TCM

In order to study the influence of the direction angles α and β on ΔV_{TCM}, we fix an error value ε of 1 m/s on the magnitude of Δv_{d}, and a value of 2 days for t_{TCM}. In this situation, all the TCMs corresponding to any $(\alpha, \beta) \in [-90°, 90°] \times [-90°, 90°]$ can be computed and a new transfer trajectory reconstructed.

The results for the reference orbits of both families are represented in Fig. 28 using the body-centered velocity reference frame (ξ, η, ζ) already introduced in Fig. 3. The red dot is at the origin of the reference frame, and the bold black arrow gives the direction of the current inertial velocity V_{TCM}. It is important to note that the initial velocity is not at the same scale as the remaining data of the plot. The grey plane represents the instantaneous orbital plane, and is perpendicular to the ζ-axis. The thinner blue arrow shows the direction of the minimum correction maneuver $\Delta V_{\mathrm{TCM}}^*$, and its length is $\Delta V_{\mathrm{TCM}}^* = \|\Delta V_{\mathrm{TCM}}^*\|$. The length of this arrow has been taken as the radius of the hemisphere that represents all the feasible directions of ΔV_{TCM}. The points on this hemisphere are colored according to the value of ΔV_{TCM} and the colorbar attached to the plot. The additional colored surface, represented behind the hemisphere, is obtained taking as modulus of the points on it the value of ΔV_{TCM}, instead of the value of $\Delta V_{\mathrm{TCM}}^*$ used for the radius of the hemisphere, and has been also colored according to the ΔV_{TCM} value. This almost planar surface is tangent to the hemisphere at the point corresponding to $\Delta V_{\mathrm{TCM}}^*$. On this surface, the points associated with too large maneuvers are excluded, and the surface is clipped by the boundaries of the box used for its representation. We want to point out that, because of the symmetric property already mentioned in Section 6.2, the hemisphere represents the results obtained for all the feasible directions, and not only of the ones associated to the values $(\alpha, \beta) \in [-90°, 90°] \times [-90°, 90°]$.

As is shown in Fig. 28, all the feasible values of ΔV_{TCM} define a two-dimensional surface, $\mathcal{M}$, in the velocity space. Adding V_{TCM} to each $\Delta V_{\mathrm{TCM}} \in \mathcal{M}$ is equivalent to translate $\mathcal{M}$ along V_{TCM}. So, in the tangent space of a configuration point X_{TCM}, the stable manifolds of all the attainable LPOs lay on a two-dimensional surface. The effect of a ΔV_{TCM} is to locate
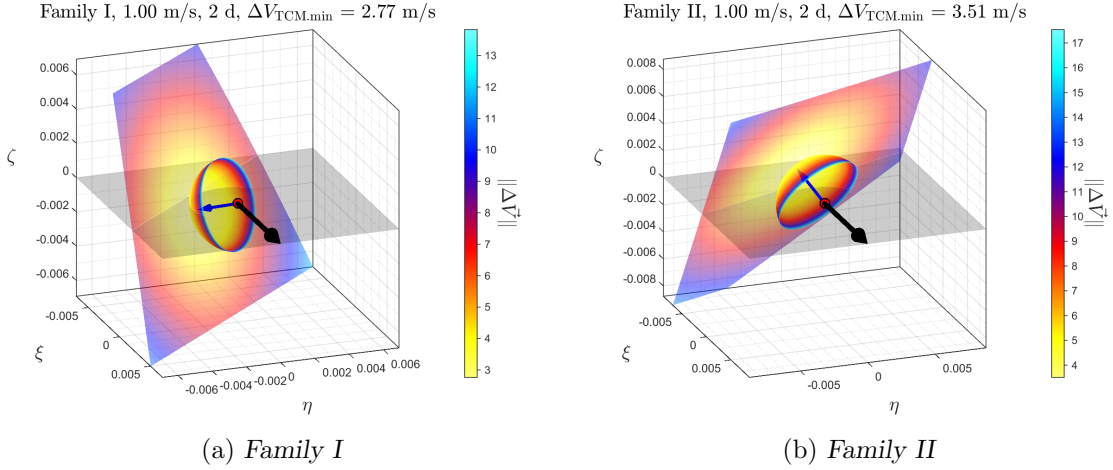
Figure 28: Using the body-centered velocity reference frame (ξ, η, ξ), values of the correction maneuver $\Delta \boldsymbol{V}_{\text{TCM}}$ for $t_{\text{TCM}} = 2$ days and $\varepsilon = 1$ m/s. The bold black arrow shows the current velocity $\boldsymbol{V}_{\text{TCM}}$, which is also the direction of the ξ-axis. The hemisphere shows all the feasible directions of $\Delta \boldsymbol{V}_{\text{TCM}}$ explored, they are colored according to ΔV_{TCM} value. The blue arrow shows the local minimum corresponding to $\Delta \boldsymbol{V}_{\text{TCM}}^*$. The surface is the extension of the hemisphere by replacing the uniform distance to the origin by the real ΔV_{TCM} along each direction.

the current $\boldsymbol{V}_{\text{TCM}}$ on this surface; since locally it is almost planar, there is only one local minimum $\Delta \boldsymbol{V}_{\text{TCM}}^*$, which has the closest distance to $\mathcal{M}$. In practice, a local optimization routine can be employed to easily find this extremum more efficiently than the grid search procedure that we have used.

According to Fig. 27, the selected transfer orbit of *Family I* needs, approximately, 22m/s less of ΔV_{d} than the one of *Family II* and, according to Fig. 28 where t_{TCM} has been fixed to 2 days, we see that *Family I* requires also a smaller TCM. As a consequence, it seems that, leaving aside practical constraints, the direct transfer of *Family I* is a better option than the one in *Family II* (we recall that both of them give a similar transfer trajectory, which is close to the one used by the CE-2 spacecraft). Furthermore, it is very likely that this conclusion can be generalized to other pairs of transfer trajectories, one in each family, with similar paths and final LPOs.

Finally, we would like to remark that all the $\Delta \boldsymbol{V}_{\text{TCM}}$ of this section are constrained to a reasonable magnitude and require a similar transfer time t_{FT} to the one of the nominal transfer shown in Fig. 27. However, if we loose these constraints, multiple solutions can be found at each point, with various t_{FT} and $\Delta \boldsymbol{V}$, similar to what we already observed in Figs. 5 and 6.

6.4.2 Influence of t_{TCM} and the initial velocity error ε in the cost of the TCM

In this section, the values of the delayed time t_{TCM} and the initial velocity error ε will be allowed to vary from 1 to 12 days, and from -1.15 to 1.15 m/s, respectively. For these ranges of values $(t_{\text{TCM}}, \varepsilon)$, the direction hemisphere of possible correction velocities is again

parameterized by (α, β) and explored to determine the optimal $\Delta \boldsymbol{V}^*_{\text{TCM}}$. Finally, we examine the variation of $\Delta \boldsymbol{V}_{\text{TCM}}$ with respect to these four parameters.
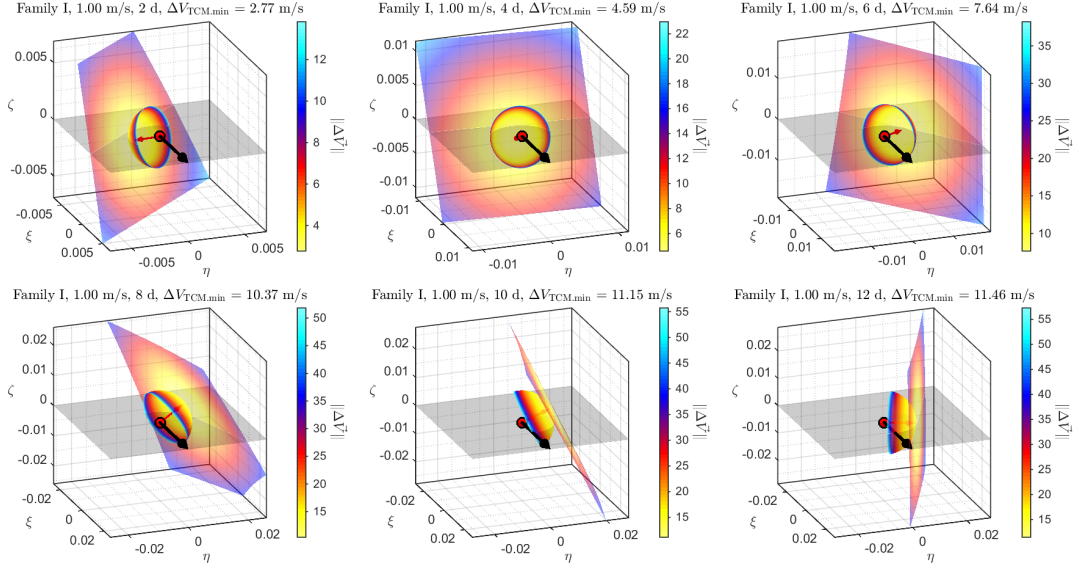

Figure 29: For the transfer orbit of *Family I*, variations of $\Delta \boldsymbol{V}^*_{\text{TCM}}$ with respect to t_{TCM} for a fixed $\varepsilon = 1.00$ m/s.

The variation of $\Delta \boldsymbol{V}^*_{\text{TCM}}$ with respect to t_{TCM}, for the transfer orbit in *Family I*, is shown in Fig. 29. In all the plots of the figure, the value of ε has been fixed to 1.00 m/s, and six different values of t_{TCM} (2, 4, 6, 8, 10 and 12 days) have been used. We remark that the range of values in the color bar for $\|\Delta \boldsymbol{V}\|$ vary from one plot to another.

From this figure it follows that the surface $\mathcal{M}$ exists in all the cases and rotates around the origin. It is interesting to note that in the last two plots, for $t_{\text{TCM}} = 10$ and 12 days, the velocity vector crosses $\mathcal{M}$ and thus $\Delta \boldsymbol{V}^*_{\text{TCM}}$ accelerates the trajectory. In all the other situations the $\Delta \boldsymbol{V}^*_{\text{TCM}}$ decelerates, which is natural since the initial velocity error ε is positive.

Fig. 30 shows the results obtained for the transfer orbit of *Family II*. The surface $\mathcal{M}$ again exists and rotates with t_{TCM} as in the preceding case. Now the surface does not show intersections with $\boldsymbol{V}_{\text{TCM}}$, and all $\Delta \boldsymbol{V}^*_{\text{TCM}}$ are decelerating, at least as far as $t_{\text{TCM}} = 12$ days. It is worth to note that, for instance for $t_{\text{TCM}} = 4$ days, the surface clearly has bendings, which show that this two-dimensional manifold is indeed not a plane in the tangential space of a fixed configuration point.

A comparison between Figs. 29 and 30 reveals that, at least after $t_{\text{TCM}} = 6$ days, the $\Delta \boldsymbol{V}^*_{\text{TCM}}$ of *Family I* starts exceeding the one of *Family II*. The largest difference, around 2.8 m/s, appears at the twelfth day. Nevertheless, combined with the difference of the initial maneuver ΔV_{d}, the transfer of *Family I* is still better for $\varepsilon = 1.00$ m/s. Of course, the earlier the first TCM is planned, the better it will be.

Next we consider the influence of the initial velocity error ε on the cost of the TCM. According to [11], and using a simplified RTBP as dynamical model, the relation between the magnitude of the local optimal correction $\Delta \boldsymbol{V}^*_{\text{TCM}}$ and the initial velocity error ε is linear. In this work we have obtained similar results using the full ephemeris model. The results for both families of direct transfer examples are shown in Fig. 31. In the two plots of this figure,
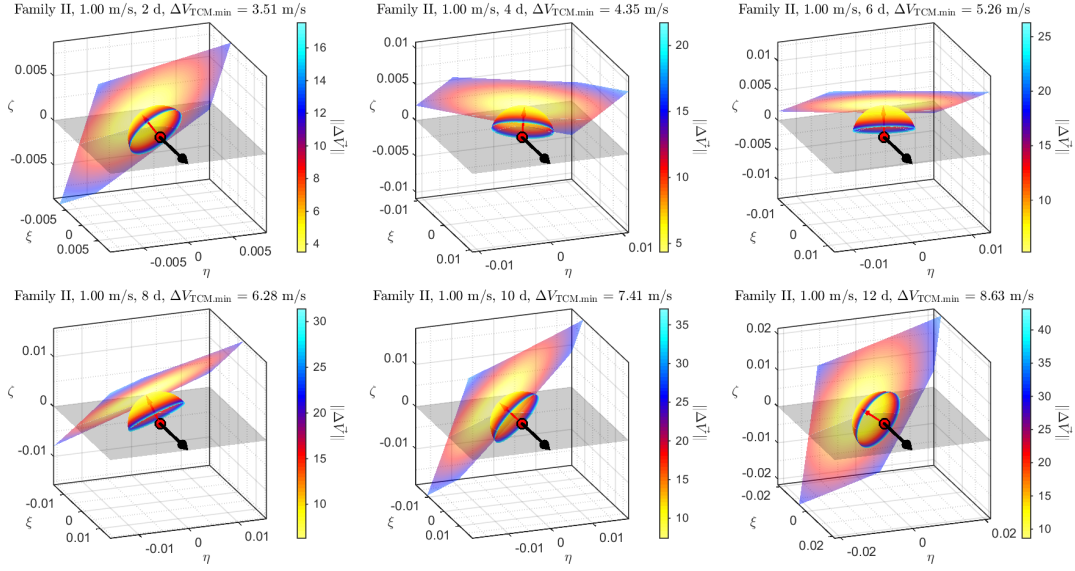
Figure 30: For the transfer orbit of *Family II*, variations of $\Delta \boldsymbol{V}^*_{\mathrm{TCM}}$ with respect to t_{TCM} for a fixed $\varepsilon = 1.00$ m/s.

the initial velocity error ε is represented in the horizontal axis, and the vertical axis shows the magnitude of the local optimal trajectory correction maneuver $\Delta \boldsymbol{V}^*_{\mathrm{TCM}}$. Different curves represent various t_{TCM} as is annotated in the caption. They clearly display a linear relation between ε and $\|\Delta \boldsymbol{V}^*_{\mathrm{TCM}}\|$.
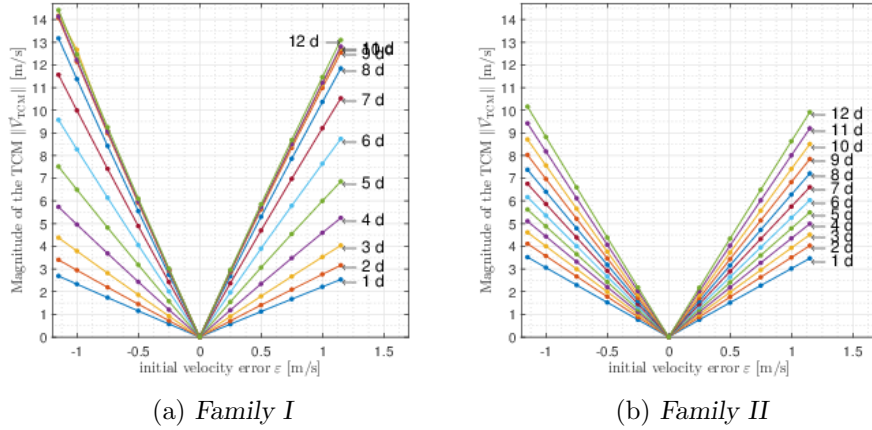

(a) *Family I*   (b) *Family II*

Figure 31: Relation between the local optimal correction maneuver $\Delta \boldsymbol{V}^*_{\mathrm{TCM}}$ and the initial velocity error ε for the transfer examples of *Families I* and *II*.

For the transfer of *Family I*, displayed on the left plot, the lines corresponding to $t_{\mathrm{TCM}} = 8$ to 12 days are very close to each other, meaning that the optimal TCM is not sensitive to the value of t_{TCM} in this time interval. As is shown in Fig. 27, during this time interval the spacecraft is very close to the Moon, so the Moon stabilizes the transfer orbit, in the sense of the relatively steady $\Delta \boldsymbol{V}^*_{\mathrm{TCM}}$ curves. It should also be noticed that even the largest $\Delta \boldsymbol{V}^*_{\mathrm{TCM}}$

value in *Family II* is about 20% less than the corresponding value in *Family I*. Finally, it can be concluded that a direct transfer in *Family I* is better than a similar one in *Family II*. If the first TCM is planned not too late after departure, $\Delta V^*_{\mathrm{TCM}}$ in *Family I* is smaller, otherwise, even though $\Delta V^*_{\mathrm{TCM}}$ is larger, the initial departure maneuver ΔV is smaller enough to compensate this extra cost.

6.4.3 Impact of t_{TCM} and velocity error direction on the TCM cost

In this section we investigate the influence on the magnitude of the TCM due to the time delay t_{TCM} and the direction of the departure velocity error. We assume that the velocity error $\Delta \boldsymbol{V}_{\mathrm{d}}$ follows a normal distribution with 1.15 m/s (3σ) along the tangential direction and 0.15 m/s (3σ) along the cross-track direction. The time delay t_{TCM} taking values between 2 and 11 days.

To evaluate the distribution of the magnitude of the TCM, a Monte-Carlo simulation has been done with 100 different initial velocity errors. The minimum, maximum, average, and standard deviation values of the TCM are listed in Table 2. The results show that short transfers are not very sensitive to the velocity errors and increase slowly with t_{TCM}. On the contrary, the range of values of the TCM for long transfers is wide, for any value of t_{TCM}, and its magnitude increases fast with t_{TCM}. The average value for a 11-day delay is about 1.3 m/s, for short transfers, and 9.0 m/s for long transfers.

Table 2: Statistics of the optimal TCM obtained in the Monte-Carlo simulations for the transfer examples of *Family I* and *II*.

	Family I				*Family II*			
Delayed time (days)	Average (m/s)	Min (m/s)	Max (m/s)	Standard deviation (m/s)	Average (m/s)	Min (m/s)	Max (m/s)	Standard deviation (m/s)
3	0.655	0.003	2.423	0.518	5.327	0.075	19.661	4.189
4	0.726	0.004	2.674	0.573	6.832	0.096	25.686	5.403
5	0.768	0.004	2.823	0.606	7.855	0.109	32.403	6.456
6	0.863	0.005	3.171	0.680	8.138	0.112	34.519	6.766
7	0.929	0.005	3.596	0.744	8.119	0.112	35.038	6.795
8	1.047	0.005	3.844	0.824	8.120	0.112	34.885	6.789
9	1.121	0.006	4.117	0.883	8.246	0.114	35.138	6.836
10	1.202	0.006	4.414	0.947	8.541	0.119	36.209	7.055
11	1.290	0.007	4.735	1.016	9.007	0.123	38.249	7.437

7 Conclusions

In this paper we have analyzed transfer opportunities from lunar orbits to Sun-Earth libration point orbits, involving a single impulsive departure maneuver. The model considered has been given by the JPL Sun-Earth-Moon ephemeris, while the transfer trajectory used by the Chang'e-2 mission has been used as a reference case for the discussion.

The explorations of the study have been carried out with a numerical approach based on a grid search and a bisection procedure. This method has been also employed to enlarge the time length of the final libration point orbit inside the libration point region, and in fact,

it also serves to compute a natural LPO inside the region, as well as to design trajectory correction maneuvers in the last part of the study.

Considering the state of CE-2 in its near polar lunar orbit, a huge number of transfer opportunities have been identified and the periodic distribution of the transfer opportunities along the whole year 2011 has been categorized and analyzed. The resulting transfers are roughly classified in direct and multi-encounter transfers. Direct transfers have a time of flight less than 43 days and have drawn most of our attention. The final LPO reached for all direct transfers are classified by a single parameter that distinguishes between halo, quasihalo and Lissajous orbits. Direct transfers appear to be clearly distributed in two families that alternate according to the phase of the Moon, and generally speaking, transfers in *Family I* usually need smaller departure maneuvers but longer time of flight than those in *Family II*.

A deeper analysis confirmed that all three kinds of LPO (halo, quasihalo and Lissajous) are detected inside these families, however, most of the reached LPOs are quasi-halo and Lissajous orbits. Final halo orbits are rare and need of larger departure maneuvers. The dependence of the transfer opportunities with respect to the initial conditions of the departure orbit has been also analyzed by means of its orbital elements. Accounting for almost circular lunar orbits, the altitude has a previsible impact on the Δv while the patterns of families I and II exhibit interesting behaviors depending on the inclination and on the longitude of the ascending node. In general, near polar orbits exhibit a marked seasonal behavior in *Family II* that it is attached to the value of the ascending node, while for departing lunar orbits with inclinations near $0°$ or $180°$, this seasonal behavior disappears. However, due to the retrograde motion, the minimum transfer costs associated with the family for $i = 180°$, are bigger than the ones for $i = 0°$.

The results of the analysis performed for a Metonic cycle indicate that, for a given fixed pair (i, Ω) considered in the year 2011, the transfer opportunities found for this year follow a periodic behavior across the years which leads to the same 2011 pattern after 19 years. In particular, the seasonal dependence exhibited for near polar orbits, basically remain about the same calendar days across the years, being only slightly shifted because the length disagreement between the calendar months and the synodic period of the Moon. Moreover, during the cycle, the Δv cost and the transfer times are kept always bounded inside the same values for both families. All these dependences provide us with a clear picture of the transfer opportunities one can have for any year. We just need to consider the pair (i, Ω) and the position of the year inside the Metonic cycle, while correcting the Δv scale just by means of considering the variation of Keplerian energy about the Moon for an altitude other than the one of CE-2.

A preliminary analysis of the TCM1 for two transfer test examples (one in each family) has been also included. Except for a few days after departure, the results indicate that *Family I* requires a larger TCM than *Family II*, but since *Family II* requires less escaping maneuver around the Moon, the overall transfer cost in *Family I* is superior than the ones in the *Family II*. Moreover, there is only one local optimal trajectory correction maneuver at each specific point given by t_{TCM}, which leads the trajectory to a new, but similar, final LPO.

Acknowledgments

References

[1] B. Barden, K. C. Howell, and M. W. Lo. Application of dynamical systems theory to trajectory design for a libration point mission. In Astrodynamics Conference, pages 268–281. American Institute of Aeronautics and Astronautics, 1996.

[2] E. Canalias, G. Gómez, M. Marcote, and J. J. Masdemont. Assessment of mission design including utilization of libration points and weak stability boundaries. Technical report, European Space Agency, 2004.

[3] E. Canalias and J. J. Masdemont. Computing natural transfers between Sun-Earth and Earth-Moon Lissajous libration point orbits. Acta Astronautica, 63:238–248, 2008.

[4] K. E. Davis, R. L. Anderson, D. J. Scheeres, and G. H. Born. The use of invariant manifolds for transfers between unstable periodic orbits of different energies. Celestial Mechanics and Dynamical Astronomy, 107(4):471–485, 2010.

[5] R. W. Farquhar, D. W. Dunham, Y. Guo, and J. V. McAdams. Utilization of libration points for human exploration in the Sun-Earth-Moon system and beyond. Acta Astronautica, 55(3-9):687–700, 2004.

[6] G. Gómez, K. C. Howell, J. J. Masdemont, and C. Simó. Station-Keeping Strategies for Translunar Libration Point Orbits. In Proceedings of the AAS/AIAA Spaceflight Mechanics Conference 1998, pages 949–967. American Institute of Aeronautics and Astronautics, 1998.

[7] G. Gómez, A. Jorba, J. J. Masdemont, and C. Simó. Study of the transfer from the Earth to a halo orbit around the equilibrium point L1. Celestial Mechanics & Dynamical Astronomy, 56(4):541–562, 1993.

[8] G. Gómez, A. Jorba, J. J. Masdemont, and C. Simó. Dynamics and Mission Design Near Libration Points - Volume III: Advanced Methods forCollinear Points. World Scientific Monograph Series in Mathematics: Volume 2. World Scientific Publishing Company, 2001.

[9] G. Gómez, W. S. Koon, M. W. Lo, J. E. Marsden, J. J. Masdemont, and S. D. Ross. Invariant Manifolds, the Spatial Three-Body Problem and Space Mission Design. In AIAA/AAS Astrodynamics Specialist Meeting, 2001.

[10] G. Gómez, W. S. Koon, M. W. Lo, J. E. Marsden, J. J. Masdemont, and S. D. Ross. Connecting orbits and invariant manifolds in the spatial restricted three-body problem. Nonlinearity, 17(5):1571–1606, 2004.

[11] G. Gómez, M. Marcote, and J. J. Masdemont. Trajectory correction manoeuvres in the transfer to libration point orbits. Acta Astronautica, 56(7):652–669, 2005.

[12] G. Gómez and J. J. Masdemont. Some zero cost transfers between libration point orbits. In AAS/AIAA Astrodynamics Specialist Conference, 2000.

[13] G. Gómez and J. M. Mondelo. The dynamics around the collinear equilibrium points of the RTBP. Physica D: Nonlinear Phenomena, 157(4):283–321, 2001.

[14] K. C. Howell and L. A. Hiday-Johnston. Time-free transfers between libration-point orbits in the elliptic restricted problem. Acta Astronautica, 32(4):245–254, 1994.

[15] K. C. Howell and M. Kakoi. Transfers between the Earth-Moon and Sun-Earth systems using manifolds and transit orbits. Acta Astronautica, 59(1-5):367–380, 2006.

[16] W. S. Koon, M. W. Lo, J. E. Marsden, and S. D. Ross. Heteroclinic connections between periodic orbits and resonance transitions in Celestial Mechanics. Chaos: An Interdisciplinary Journal of Nonlinear Science, 10:427–469, 2000.

[17] W. S. Koon, M. W. Lo, J. E. Marsden, and S. D. Ross. Shoot the moon. In Spaceflight mechanics 2000, pages 1017–1030, 2000.

[18] W. S. Koon, M. W. Lo, J. E. Marsden, and S. D. Ross. Low energy transfer to the Moon. In Dynamics of Natural and Artificial Celestial Bodies, pages 63–73. 2001.

[19] B. Le Bihan, J. J. Masdemont, G. Gómez, and S. Lizy-Destrez. Invariant manifolds of a non-autonomous quasi-bicircular problem computed via the parameterization method. Nonlinearity, 30(8):3040–3075, 2014.

[20] B. Le Bihan, J. J. Masdemont, G. Gómez, and S. Lizy-Destrez. Systematic study of the connections between the collinear libration points of a coherent Sun-Earth-Moon restricted four-body model. In Proceedings of the 68th International Astronautical Congress, pages 1–14. International Astronautica Federation (IAC Papers Archive System), 2017.

[21] Y. Lian, G. Gómez, J. J. Masdemont, and G. Tang. A note on the dynamics around the Lagrange collinear points of the Earth–Moon system in a complete Solar System model. Celestial Mechanics and Dynamical Astronomy, 115(2):185–211, 2013.

[22] L. Liu, Y. Liu, J.-f. Cao, S. Hu, G. Tang, and J.-f. Xie. CHANG'E-2 lunar escape maneuvers to the Sun–Earth L2 libration point mission. Acta Astronautica, 93:390–399, 2014.

[23] M. Nakamiya and Y. Kawakatsu. Transfer Trajectories from the Moon to Sun-Earth Halo Orbits. Journal of Guidance, Control, and Dynamics, 37(3):1000–1003, 2014.

[24] M. Nakamiya, D. J. Scheeres, H. Yamakawa, and M. Yoshikawa. Analysis of Capture Trajectories into Periodic Orbits About Libration Points. Journal of Guidance, Control, and Dynamics, 31(5):1344–1351, 2008.

[25] J. S. Parker and M. W. Lo. Shoot the Moon 3D. In AAS/AIAA Astrodynamics Specialist Conference, 2005.

[26] H. Peng, X. Bai, J. J. Masdemont, G. Gómez, and S. Xu. Libration Transfer Design Using Patched Elliptic Three-Body Models and Graphics Processing Units. Journal of Guidance, Control, and Dynamics, 40(12):3155–3166, 2017.

[27] H. Peng, Y. Qi, S. Xu, and Y. Li. Numerical energy analysis of the escape motion in the elliptic restricted three-body Problem. In AAS/AIAA Spaceflight Mechanics Conference 2015, pages 1–19, Williamsburg, VA, 2015.

[28] Y. Qi and A. de Ruiter. Study of Correction Maneuver for Lunar Flyby Transfers in the Real Ephemeris. Journal of Guidance, Control, and Dynamics, 41(10):2112–2132, 2018.

[29] D. Qiao, P. Cui, Y. Wang, J. Huang, L. Meng, and D. Jie. Design and analysis of an extended mission of CE-2: From lunar orbit to Sun–Earth L2 region. Advances in Space Research, 54(10):2087–2093, 2014.

[30] V. G. Szebehely. Theory of Orbits - The Restricted Problem of Three Bodies. Academic Press, 1967.

[31] Y. Wang, D. Qiao, and P. Cui. Analysis of Two-Impulse Capture Trajectories into Halo Orbits of Sun–Mars System. Journal of Guidance, Control, and Dynamics, 37(3):985–990, 2014.

[32] W. Wu, Y. Liu, L. Liu, J.-l. Zhou, G. Tang, and Y. Chen. Pre-LOI trajectory maneuvers of the CHANG'E-2 libration point mission. Science China Information Sciences, 55(6):1249–1258, 2012.